THE INTENSIFICATION OF NORTHERN COMPONENT DEEP WATER FORMATION DURING THE MID-PLEISTOCENE CLIMATE TRANSITION

by

Robert K. Poirier

A thesis submitted to the Faculty of the University of Delaware in partial fulfillment of the requirements for the degree of Master of Science in Marine Studies

Fall 2013

THE INTENSIFICATION OF NORTHERN COMPONENT DEEP WATER FORMATION DURING THE MID-PLEISTOCENE CLIMATE TRANSITION

by

Robert K. Poirier

Approved: _____

Katharina Billups, Ph.D.
Professor in charge of thesis on behalf of Advisory Committee

Approved: _____

Nancy Targett, Ph.D.
Dean of the College of Earth, Ocean, and Environment

Approved: _____

James G. Richards, Ph.D.
Vice Provost for Graduate and Professional Education

ACKNOWLEDGEMENTS

There are many people I would like to thank in the completion of this work. First, I would like to acknowledge my undergraduate advisor's Dr. Rowan Lockwood and Dr. Thomas M. Cronin for providing me the first opportunities to explore my interest in paleoclimatology and paleoceanography. They were both instrumental in providing me with the skills and knowledge that have helped me get to where I am today. To Dr. Katharina Billups, I owe many thanks for taking me on as a graduate student, being a great hands-on instructor, and allowing me to explore my own interests within her pre-existing project at ODP Site 1063. Professional gratitude goes to Dr. Mirium Katz, Dr. William Ullman, and Dr. Chris Sommerfield for agreeing to serve on my committee, and for their guidance based on their individual areas of expertise. I would like to thank Jessi Wenke and Dr. Nick Venti for helping me wash some of the 700+ sediment samples used for this study. Also, thanks to Andre Scheinwald for being a great lab mate and for putting up with my taking over so much of the countertop space in the lab. Last but certainly not least, I would also like to thank my family, friends, and all of the outstanding members of the faculty and staff within the program who have made graduate school a great experience from start to finish. I would like to sincerely thank the family of Marian R. Okie and the Oceanography program for funding my first and second year within the program, respectfully.

TABLE OF CONTENTS

LIST OF TABLES

LIST OF FIGURES

ABSTRACT

This work examines the deep-water hydrography at Ocean Drilling Program (ODP) Site 1063 (subtropical North Atlantic, ~4600m) throughout the mid Pleistocene climate transition (MPT) by using high resolution benthic stable isotope ($\delta^{18}O$, $\delta^{13}C$) analyses from ~500 to 750 ka (Marine Isotope Stages [MIS] 13-18). The record fills a gap in published records creating a continuous composite stable isotope time series from ~250 to 1000 Ka (MIS 8-29). The benthic foraminiferal $\delta^{18}O$ composite provides age control through tuning to the global stack of Lisiecki and Raymo [2005]. The benthic foraminiferal $\delta^{13}C$ record provides a proxy for changes in the relative flux of the lower-most component of northern-sourced deep waters from MIS 8 to MIS 29. Comparison of the $\delta^{13}C$ record with others from the Atlantic basin indicates that a unique increase occurred in the interglacial $\delta^{13}C$ values recorded at Site 1063 at ~700 ka (MIS 17). While interglacial $\delta^{13}C$ values consistently overlap with those recorded in the deep South Atlantic prior to this time, they consistently approach those recorded in the deep North Atlantic thereafter. By comparing the Site 1063 data to 16 other published records from sites throughout the Atlantic Ocean, I deduce that an initial enhancement of NADW production likely occurred within MIS 19, not affecting the deepest region of the North Atlantic until MIS 17. The change in deep-ocean circulation occurred without any change in orbital forcing, and pre-dates the onset of more extreme Pleistocene interglacial warmth (MIS 11) by 300-400 kyr. These results provide new evidence for the northwest migration of the interglacial Arctic Front position during this time, likely relating to Eurasian ice sheet dynamics and intensifying glacial terminations within the Norwegian-Greenland Sea during the MPT.

Chapter 1

INTRODUCTION

The mid-Pleistocene transition (MPT) refers to the shift (~1.2 Ma to 600 ka) from 41-kyr obliquity-driven climate cycles, to the higher amplitude, quasi-periodic low frequency (~100kyr) glacial cycles. The low-frequency glacial cycles that began during the MPT are most likely driven by precession (23 kyr period), with each glacial termination defined by the fourth or fifth precession cycle [Head & Gibbard, 2005; Maslin & Ridgewell, 2005; Head et al., 2008]. Prior to the MPT, early Pleistocene glacial cycles responded linearly (directly) to obliquity forcing at a period of 41-kyr [Imbrie et al., 1992]. However, the ~100-kyr cycles following the MPT appear to respond non-linearly (various feedback responses) to orbital forcing [Imbrie et al., 1993], indicating a change to the Earth's global internal feedback climate response [Head & Gibbard, 2005; Clark et al., 2006; Head et al., 2008]. Most hypotheses for the origin of the MPT involve a response to the long-term cooling since the middle Eocene [Zachos et al., 2001], driven by such possible mechanisms as ice-sheet dynamics [Clark & Pollard, 1998; Clark et al., 2006] or a secular decline in atmospheric CO_2 [Raymo et al., 1997; Saltzman, 2001; Ruddiman & Raymo, 2003]. Other less discussed hypotheses exist, considering a change in location of deep-water formation in the Northern Hemisphere [Denton, 2000], or the destabilization and release of gas hydrates on continental margins [Kennett et al., 2003]. To date, no consensus has been reached on one mechanism adequately explaining this shift from linear 41-kyr glacial cycles to the non-linear 100-kyr glacial cycles of the last ~700-kyr.

Studying deep-water circulation is integral in paleoclimate reconstructions, because the

ocean-air interactions that drive this circulation further regulate global heat distribution, and therefore climate, especially within the North Atlantic [Schmitz & McCartney, 1993]. Generally, interglacial deep-water circulation is largely driven by strong production of North Atlantic Deep Water (NADW), with the water mass penetrating into the deep South Atlantic between ~2000 and 4000m. Below ~4000-4500m, the denser, southern-sourced Antarctic Bottom Water (AABW) underlies the NADW. During glacial periods, production of the lower component of NADW ceases, while a more intermediate limb of NADW persists (~1000-2000m). This diminished NADW production reflects the decreased transport of warm surface waters to the high northern latitudes during glacial periods, and allows strong advection of AABW into the deep North Atlantic Ocean. The strength of production of these waters masses relative to one another drives the global redistribution of heat. A decrease in NADW production during the MPT is thought to have lasted until the onset of higher amplitude glacial cycles at ~400ka (MIS 11) [Raymo et al., 1990; Raymo et al., 1997].

Here, I hypothesize that a distinct change occurred causing the intensification of formation of the lower-most component of NADW between ~500 to 750ka, during the MPT. If true, this change would have occurred well before 400ka, as assumed by Raymo et al. [1997], and would imply a more direct link between deep-water circulation and the MPT itself. To test this hypothesis, I constructed stable isotope records ($\delta^{18}O$ and $\delta^{13}C$) from Ocean Drilling Program (ODP) Site 1063 (34°N, 58°W, 4583m). Site 1063 is located near the mixing zone between NADW and AABW in the modern subtropical North Atlantic Ocean [Keigwin et al., 1998]. Site 1063 is the deepest site for which such data have been published from the North Atlantic to-date. Records from Site 1063 can be used to determine the strength of these water masses relative to one another on orbital and millennial timescales [Poli et al., 2000; Ferretti et

al., 2005; Billups et al., 2011; Thornally et al., 2013]. By comparing results from Site 1063 to other sites throughout the deep Atlantic Ocean, this study provides new insight to the response of deep ocean circulation to the climatic reorganization that occurred during the MPT.

Chapter 2

BACKGROUND

2.1 The mid-Pleistocene Climate Transition

The Pleistocene epoch began around 2.6 Ma and is defined by repeated cycles of glaciation at polar latitudes in both hemispheres. The distinct differences between Pleistocene glacial and interglacial oxygen isotope values led to the identification of various periods as Marine Isotope Stages (MIS), with odd and even numbered stages representing interglacial and glacial periods, respectfully [Emiliani, 1955; Shackleton, 1967; Broecker & van Donk, 1970]. Up until ~1.2 Ma, glacial cycles were characteristically dominated by the 41-kyr obliquity orbital periodicity [Imbrie et al., 1992]. The period known as the mid-Pleistocene transition (MPT) began around 1.2 Ma and lasted until ~700 ka [Clark et al., 2006] (~500 ka [Head et al., 2008]). During this time, symmetric 41-kyr cycles gave way to the asymmetric 100-kyr cycles of the late Pleistocene [Imbrie et al., 1993]. This transition is perhaps most evident in the LR04 global benthic stack where Lisiecki and Raymo [2005] compiled benthic oxygen isotope records from 57 globally distributed sites (Figure 2.1).

Prior to the MPT, the symmetrical shape of 41-kyr cycles suggests a climate response linearly related to forcing associated with changes in obliquity [Imbrie et al., 1992]. Originally, the 100-kyr cycles of the late Pleistocene were thought to correspond to orbital forcing associated with the Milankovich hypothesis, whereby insolation changes due to orbital eccentricity were responsible for glacial cycles [Hays et al., 1976]. However, that hypothesis could neither explain the emergence of 100-kyr climate cycles in the absence of a change in orbital forcing [Berger & Loutre, 1991], nor

its subsequent dominance of orbital-scale climate variability when known forcing at the eccentricity frequency is the weakest of the three orbital variations [Shackleton & Opdyke, 1976; Head & Gibbard, 2005; Maslin & Ridgewell, 2005; Clark et al., 2006; Head et al., 2008]. Another orbital forcing mechanism has been proposed, whereby the 100-kyr periodicity of the angle of Earth's orbital plane (known as orbital inclination), governs the observed 100-kyr glacial interglacial cycles [Muller & MacDonald, 1997]. However, the proposed governing effect of orbital inclination whereby the Earth passes through increased amounts of dust in space is not thought to have been sufficient to govern late Pleistocene glacial cycles [Raymo, 1997; Mudelsee & Schulz, 1997; Paul & Berger, 1999]. To date, the most widely considered explanation for the low frequency periodicity of late Pleistocene climate cycles of the late Pleistocene is that they are governed by the fourth or fifth precession cycle [Raymo, 1997; Maslin & Ridgewell, 2005; Head et al., 2008]. As eccentricity modulates the amplitude of precession cycles, it plays a role in determining whether the fourth or fifth precession cycle coincides with glacial terminations [Maslin & Ridgewell, 2005].

Perhaps the most prominent feature of late Pleistocene 100-kyr glacial cycles is their asymmetric "saw tooth" shape, defined by the slow build up of ice followed by subsequent rapid melting (Figure 2.1). This pattern is indicative of a non-linear response of the climate system to orbital forcing [Imbrie et al., 1993; Maslin & Ridgewell, 2005]. A non-linear response indicates a change in Earth's global internal feedback climate system [Head & Gibbard, 2005; Clark et al., 2006; Head et al., 2008]. Such internal feedbacks are the result of the Earth system amplifying and transforming changes in insolation received at Earth's surface, and can occur in various ways. For example, the classic 'ice albedo' feedback is a positive feedback mechanism whereby the accumulation of ice and snow increases the reflectivity of Earth's surface, reducing its absorption

efficiency and causing lower temperatures. These lower temperatures then cause more snow and ice to accumulate, further perpetuating the positive response.

Another example of a feedback response occurs during rapid deglaciations caused by the natural instability of ice sheets. Deglaciations, also known as glacial terminations of the late Pleistocene, are the periods of time when the global climate state rapidly shifts from full glacial conditions, to full interglacial conditions at the end of an ~100-kyr glacial cycle. An initial increase in summer insolation at 65^{o}N [Imbrie et al., 1993] provides melting and initial retreat of ice sheets from their glacial maximum extents. Additionally, the rise of atmospheric CO_2 and CH_4 further promotes warming and melting of large continental ice sheets [Shackleton, 2000; Ruddiman & Raymo, 2003]. These forcing mechanisms produce rising sea levels, which undercut large ice sheets adjacent to the oceans, increasing sea-level further [Maslin et al., 2001; Maslin & Ridgewell, 2005]. This sea-level feedback mechanism can be extremely rapid [Fairbanks, 1989; Maslin & Ridgewell, 2005], and perhaps drives the rapid collapse of ice sheet margins at or below base level [Denton et al., 2010]. These mechanisms for rapid deglaciation produce one end of the 'saw-tooth' climate signal typical of late Pleistocene glacial cycles [Maslin & Ridgewell, 2005].

The MPT is widely recognized as marking a major global climatic reorganization that profoundly affected ocean and atmospheric circulation, ice sheets, and the distribution and evolution of biota [Head et al., 2008]. Most hypotheses for the origin of the MPT suggest it as a response to global long-term cooling since the Eocene [Zachos, 2001], driven by such mechanisms as ice-sheet dynamics [Imbrie et al., 1993; Clark & Pollard, 1998; McClymont & Rosell-Mele, 2005; Clark et al., 2006; Bintanja & van de Wal, 2008; Hernandez-Almeida et al., 2012], deep-ocean cooling [Gildor & Tziperman, 2000; Tziperman & Gildor, 2003], and/or a secular decline in atmospheric CO_2 [Raymo et al., 1997; Saltzman, 2001; Maslin & Ridgewell, 2005]. Other less-widely discussed hypotheses

for the MPT also exist. One such hypothesis includes a shift in the area of northern deep-water formation from the Arctic Ocean to the Nordic seas due to a proposed uplift of the Greenland-Scotland submarine ridge [Denton, 2000]. Another suggests a reorganization of intermediate-depth ocean circulation causing warm waters during glacial and deglacial periods to destabilize gas hydrates on the continental margins releasing methane [Kennett et al., 2003]. Despite the topic being a major focus of research within the paleoclimate community, no one mechanism has been accepted as the driving cause of the MPT.

2.2 Modern Deep-Water Hydrography

Between the northward-flowing surface waters of the Gulf Stream (~30 to 155 Sverdrups [Sv]), and the net southerly flow of intermediate and deep (~10 to 15 Sv) waters, most of the climatically important exchanges of heat, salt, and water with other ocean basins occurs in the westernmost region of the North Atlantic (1 Sv = Sverdrup = $10^6 m^3 s^{-1}$) [Keigwin et al., 1998]. Today, the deep-Atlantic Ocean is primarily ventilated by North Atlantic Deep Water (NADW), which is partly formed by deep overflow from the Nordic Seas and partly by wintertime convection to intermediate depths (with a small contribution of Mediterranean Sea water) [McCartney & Talley, 1982; 1984]. The main, southward stretching tongue of the NADW is intensified in the western North Atlantic basin, within the Western Boundary Undercurrent (WBUC), which follows the topography of the basin, along the outer shelf of the North American continent. The deepest/densest limb of the WBUC is fed mainly by deep overflow waters from the Nordic Seas (below ~2500m), and is often termed lower North Atlantic Deep Water (LNADW) [McCartney & Talley, 1982; 1984; Dickson & Brown, 1994; Stahr & Sanford, 1999; Bower & Hunt, 2000]. When discussing the influence of NADW at ODP Site 1063

throughout this paper, I am referring to the deepest/densest limb of this LNADW. Other branches of the NADW exist in various re-circulating gyres east of the WBUC through deep-water canyons.

At the deepest levels of the western North Atlantic, Antarctic Bottom Water (AABW) flows northwards and blends with several other water masses in these deep re-circulating gyres of the NADW [Keigwin et al., 1998]. The AABW flows northward and mixes with the lower-most limbs of the NADW, near the location of ODP Site 1063. This location makes the site ideal for studying the interactions of the deepest/densest limbs of northern vs. southern sourced deep-waters in relation to changing climatic conditions.

2.3 ODP Site 1063 Lithology

The sediments recovered from Site 1063 on the northeast Bermuda Rise record the rapid deposition of clays, silts, and nannofossils documenting the dynamics of deep ocean advection and redeposition [Keigwin et al., 1998]. The uppermost lithostratigraphic unit, up to a mcd of ~170 of sediment (0 to ~885ka [MIS 21] based on age model constructed in this study – *see section 5.2*) from Site 1063 consists primarily of a cyclic alternation between biogenic silica-rich (~15-30% and occasionally exceeding 60%) and clay-rich (~70-100%) sediments (Figure 2.2) [Keigwin et al., 1998]. The persistence of one sedimentary unit, suggests that sediment focusing by deep currents has been the dominant depositional process at this site [Keigwin et al., 1998]. This section also has very distinctive "brick-red" lutite, or red layers of silt and clay, which along with the cyclical biogenic vs. clay-rich sediments, are characteristic of the uppermost sections of all the ODP Leg 172 sediment cores, providing additional lithostratigraphic correlation from site to site (Figure 2.2) [Keigwin et al., 1998]. These lutite beds are thought to reflect increased advection of fine-grained

sediment from the Nova Scotia region during cold climate intervals [Keigwin et al., 1998]. Calcareous nannofossils are the dominant microfossils within this section of core, and are generally well preserved, except for some intervals where they are dissolved [Keigwin et al., 1998]. Foraminiferal assemblages of planktonic origin are generally dissolved, revealing potential shoaling of the Carbonate Compensation Depth (CCD), currently located at depths above Site 1063 (~4500m), [Keigwin et al., 1998]. Below a mcd of ~170, the sediment is predominantly clay, nannofossil, and silt mixed sediment (Figure 2.2). This unit persists to the end of the composite record at Site 1063 (~1Ma based on the age model constructed for this study).

2.4 Previous Research at ODP Site 1063

Several previous studies have sought to determine deep-water circulation from Site 1063 using benthic foraminiferal $\delta^{13}C$ records during different time intervals (Figure 2.3). To determine the affect of millennial-scale climate variability on NADW circulation during MIS 11 and MIS 12, Poli et al. [2000] published stable isotope records from ODP Site 1063 from ~ 360 to 470 ka (Figure 2.3A). This record indicated that the bottom water mass during MIS 12 and MIS 10 had lower $\delta^{13}C$ values (~ -0.5 to -1.0 per mil), similar to records from deep sites in the South Atlantic at that time (Figure 2.3B) [Poli et al., 2000]. Alternatively, during MIS 11 $\delta^{13}C$ values were close to present-day NADW values at this depth (of ~1.0 per mil [Kroopnick, 1980] – Figure 2.3C) [Poli et al., 2000]. Poli et al. [2000] concluded that these glacial-interglacial differences reflect that the bottom water in the North Atlantic was more nutrient-enriched during glacial periods, indicating reduced NADW and increased inputs of water from a southern source region (Figure 2.3B).

Similarly, to determine orbital and millennial scale circulation changes in the early-middle Pleistocene from ~740 to 1020 ka (MIS 18 to MIS 29 – Figure 2.3A), stable isotope records from Site 1063 were published by Ferretti et al. [2005], who also noted significant northward penetration and shoaling of southern-source deep water during glaciations (Figure 2.3B). Therefore, it was determined the circulation patterns in the deep western North Atlantic were strongly influenced by southern-source water [Ferretti et al., 2005]. The measured $\delta^{13}C$ values at Site 1063 from ~740 to 1020 ka varied between ~ -2 and 0 per mil [Ferretti et al., 2005]. These values, when compared to other records from the source regions of source water in the North vs. South Atlantic, demonstrate a northward penetration of AABW, not only during glacial intervals (MIS 18, 20, 22, 24), as discussed by Ferretti et al. [2005], but also during the interglacial intervals of MIS 19, 21, 23, 25 (Figure 2.3B).

In an effort to reconstruct millennial-scale changes in deep circulation throughout two extreme interglacial (MIS 9 and MIS 11) and two extreme glacial (MIS 10 and MIS 12) periods, Billups et al. [2011] published stable isotope data from ~250 to 360 ka, incorporating the data discussed above by Poli et al. [2000]. By doing so, Billups et al. [2011] produced and discussed a complete stable isotope record from MIS 8 through MIS 13 (Figure 2.3A). During interglacial MIS 9, $\delta^{13}C$ values at Site 1063 reach up to ~0.6 to 0.7 per mil, whereas during the glacial periods (MIS 10 and MIS 8) the $\delta^{13}C$ values drop to ~ -1.0 per mil (Figure 2.3). When compared to the $\delta^{13}C$ records of sites in the North versus South Atlantic, these results infer that Site 1063 was primarily influenced by AABW (~1 per mil) during glacial periods MIS 8 and MIS 10 (Figure 2.6B), and by NADW (~0.75 per mil) during interglacial MIS 9 (Figure 2.3C).

In summary, previously published records at Site 1063 reveal several overall trends/patterns of thermohaline circulation, deep-water mass influence, and deep-water mass distribution before and

after my study interval. First, during the time period from MIS 29 to MIS 18, Site 1063 appeared to be influenced primarily by AABW during both glacial and interglacial periods (Figure 2.3B), as indicated by the $\delta^{13}C$ records of Ferretti et al. [2005]. Second, from MIS 13 to MIS 8, glacial intervals (MIS 12, MIS 10, & MIS 8) exhibited continued AABW influence at Site 1063 (Figure 2.3B), as indicated by the $\delta^{13}C$ records of Poli et al. [2000] (MIS 12 and MIS 10) and of Billups et al. [2011] (MIS 8). Lastly, it was noticed that Site 1063 was under a more predominant influence of NADW during interglacial periods after my study interval (MIS 13, MIS 11, & MIS 9). Based on the results discussed above from previous studies at Site 1063, I hypothesize that a major change in thermohaline circulation occurred within my study interval (MIS 13 to MIS 18 – Figure 2.3). This change would have allowed the deepest limb of northern-sourced NADW to establish a more dominant influence during interglacial periods over AABW at Site 1063, and throughout the deep-Atlantic Ocean. If correct, this would suggest a more direct link between the MPT and deep water circulation, providing evidence for the intensification of NADW formation well before ~400ka, as inferred by Raymo et al. [1997].

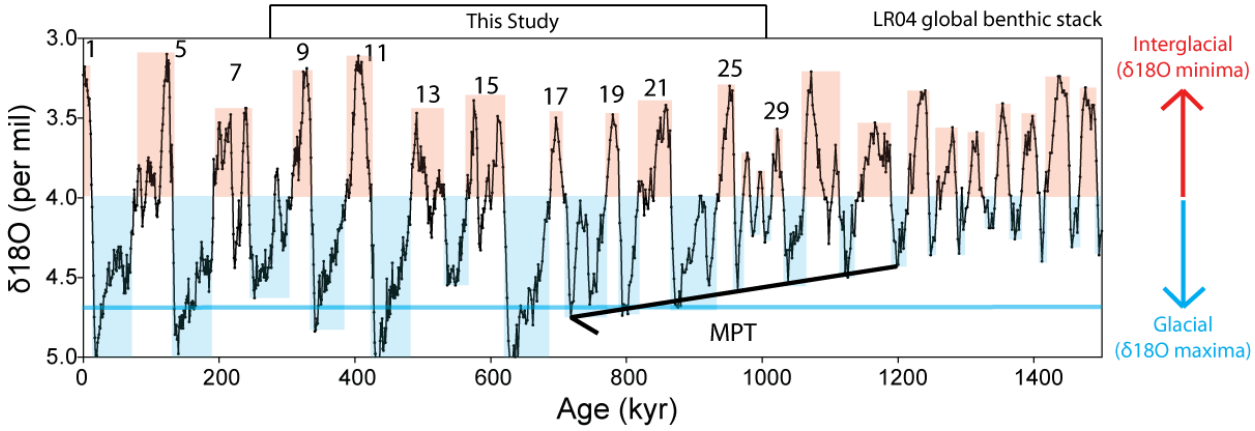

Figure 2.1: The global benthic stack of Lisiecki & Raymo [2005], with even numbered glacial Marine Isotope Stages (MIS) highlighted in blue, and odd numbered interglacial MIS periods highlighted in red. The intensification of glacial periods during the MPT is shown, associated with the growth of thicker ice sheets in the Northern Hemisphere. A potential glacial threshold in relation to the MPT is highlighted.

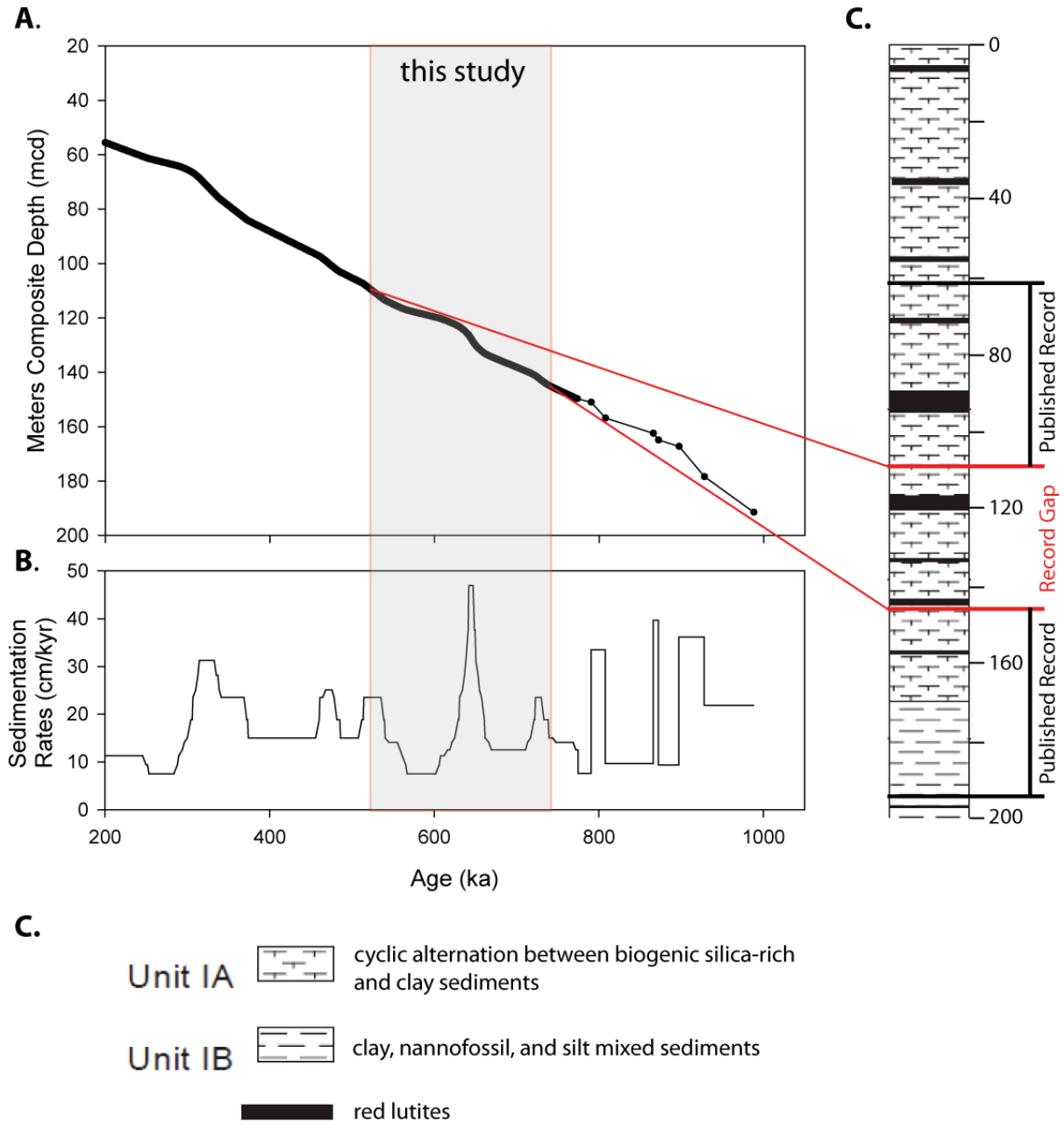

Figure 2.2: Information on the sediment core recovered from ODP Site 1063. The **A.** age vs. depth relationship and **B.** sedimentation rate information derived from the initial age model for Site 1063 by Channell et al. [2012]. **C.** A generalized core schematic from the initial cruise report for the Site 1063 sediment core highlighting the two main sedimentary units in this section, as well as the distinct red lutite layers.

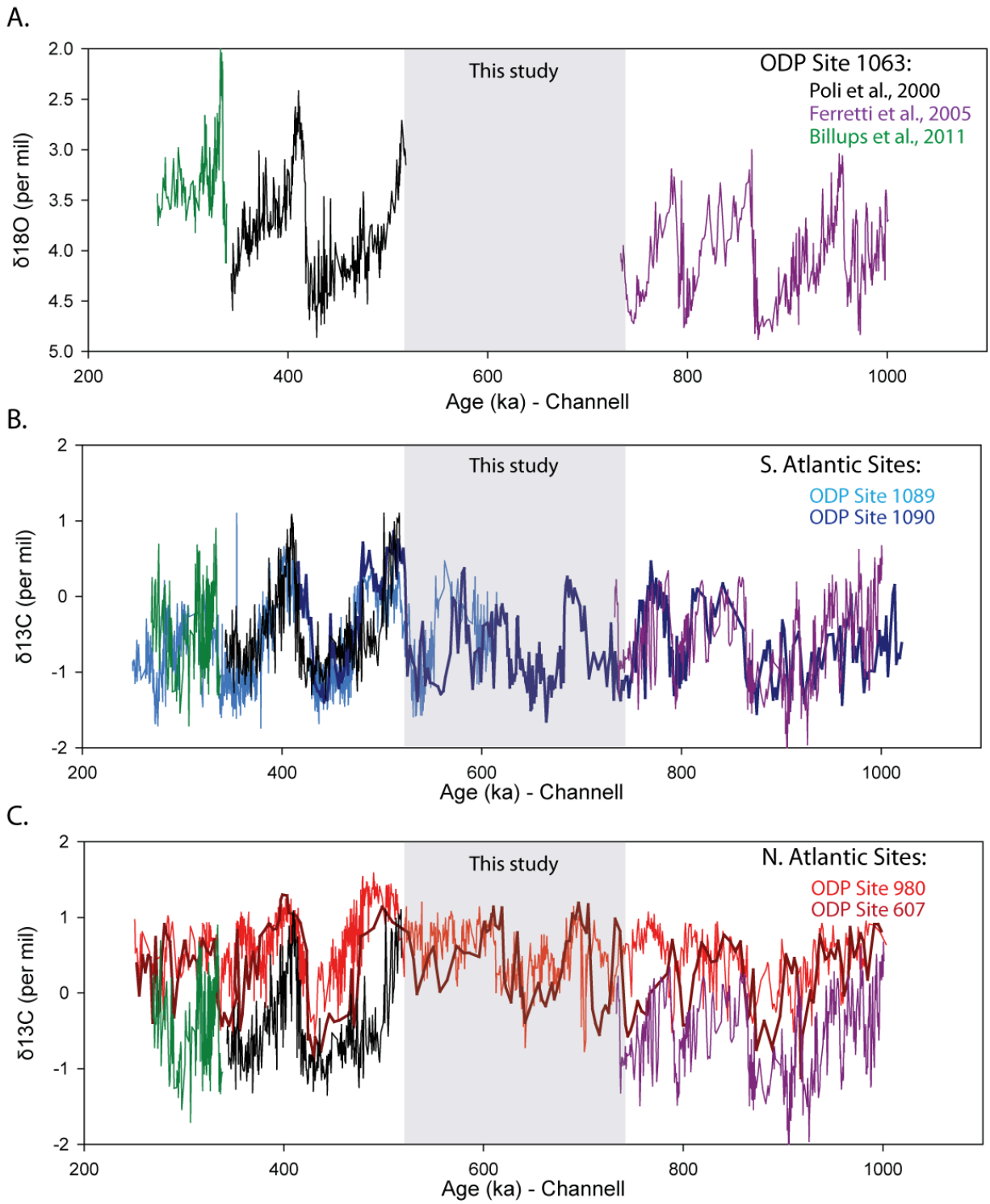

Figure 2.3: The previously published $\delta^{18}O$ (**A.**) and $\delta^{13}C$ (B. & C.) records from ODP Site 1063 of Poli et al. [2000] (black), Ferretti et al. [2005] (purple), and Billups et al. [2011] (green). The $\delta^{13}C$ records from these studies are shown **B.** in relation to those of ODP Site 1089 (4621m [Hodell et al., 2000]) and ODP Site 1090 (3700m [Becquey & Gersonde, 2002]) in the deep South Atlantic source region of AABW, and **C.** in relation to those of ODP Site 980 (2168m [Flower et al., 2000] and ODP Site 607 (3427m [Raymo et al., 1990; 1997] from the deep North Atlantic source region of NADW.

Chapter 3

RESEARCH STRATEGY

3.1 Site Selection

ODP Site 1063 is located near the mixing zone of the densest limbs of NADW and AABW in the modern ocean (Figure 3.1). This makes the site ideal to study the interactions between these two water masses through time. Additionally, the sediment recovered from ODP Site 1063 is from a sediment drift located on the northeast Bermuda Rise. Sediment drifts are widespread in the North Atlantic basin and reflect both the abundant sources of sediment and its focusing by deep currents [McCave & Tucholke, 1986; Keigwin et al., 1998]. Furthermore, these sediment drifts are ideal to be exploited for their high-resolution paleoceanographic and paleoclimatic information [Keigwin & Jones, 1994; McCave et al., 1995]. Sedimentation rates have been documented from this drift region to be as high as ~200 cm/kyr, resulting from the advection of clay and silt by the deep re-circulating gyres in the region [Keigwin et al., 1998]. Due its location on this sediment drift, ODP Site 1063 provides as one of the highest resolution archives of paleoclimate and paleoceanographic information known from the open sea [Keigwin et al., 1998]. Much of the clay and silt found at this site can be sourced from eastern Canada, and therefore studies from this location have the potential to link the marine, terrestrial, and atmospheric components of the climate system [Keigwin et al., 1998]. With high sedimentation rates, and being located between the densest limbs of the two primary deep-water masses in the North Atlantic, ODP Site 1063 is ideal for reconstructing deep-water circulation throughout the MPT.

3.2 Deep water reconstruction

In this study, I reconstruct deep-water circulation at ODP Site 1063, and throughout the deep Atlantic Ocean by determining the influence of NADW relative to AABW through time. These two water masses have very specific and distinguishable physical properties such as temperature (AABW: -1 to 2°C; NADW: 2 to 4°C) and salinity (AABW: ~34.6; NADW: ~34.9). Because temperature and salinity in conjunction do not leave a distinct imprint in the geologic record, I use benthic foraminiferal $\delta^{13}C$ values to reconstruct changes in deep-water distributions.

The distribution of $\delta^{13}C$ within oceans is controlled primarily by the interaction of biological uptake of nutrients at the sea surface (photosynthesis), air-sea gas exchange, decomposition (respiration) in deeper water masses, and mixing of water masses [Spero et al., 1991; 1997; Charles & Fairbanks, 1992; Mackensen et al., 1993; Hodell & Venz-Curtis, 2006]. The two primary surface-water sources of global deep-water formation today have preformed $\delta^{13}C$ values that can be clearly distinguished from one another [Shackleton, 1977; Clark et al., 2006]. NADW is formed at high northern latitudes from near-surface waters that have largely equilibrated with the atmosphere, and have relatively low preformed nutrients (Figure 3.1B), both of which yield high preformed $\delta^{13}C$ values of 1.0 to 1.5 per mil [Clark et al., 2006]. Alternatively, AABW formed at high southern latitudes originates from deeper upwelled waters in the circumpolar current that are only briefly exposed to the atmosphere (in addition to having limited gas exchange due to sea-ice cover) [Clark et al., 2006]. Due to this wind-driven upwelling, these waters also have high nutrient contents (Figure 3.1B), resulting in the lower preformed $\delta^{13}C$ values of ~0.3 per mil (more ^{12}C released from decomposition of organic matter) today [Clark et al., 2006]. By comparing the benthic $\delta^{13}C$ records at any given site through time

to the $\delta^{13}C$ values of NADW vs. AABW, inferred from deep records near their source regions, it is possible to reconstruct how the circulation of these two water masses in relation to one another changed through time.

However, there are two ways in which preformed $\delta^{13}C$ values of deep-water masses can be altered: mixing between water masses with different isotopic signatures, and continued remineralization of organic carbon [Mackensen et al., 1993]. The older the deep-water mass becomes as it circulates throughout the deep-ocean, the more negative its $\delta^{13}C$ value becomes as the decomposition of sinking organic matter continues, returning ^{12}C into the dissolved carbon pool. Therefore, the $\delta^{13}C$ composition of seawater cannot act as a conservative tracer of deep-water masses on a global scale. Nevertheless, within the Atlantic Ocean, the $\delta^{13}C$ distribution acts as a conservative tracer because the rates of production and degradation of organic carbon are very low [Curry et al., 1988]. This means that alterations to preformed $\delta^{13}C$ values are due mainly to the mixing of deep-water masses.

3.3 Benthic foraminifera

The primary method of determining the deep water mass present at a site through time is constructing $\delta^{13}C$ records from tests of benthic foraminifera. Benthic foraminifera secrete calcite tests ($CaCO_3$) from ocean water at or near the sediment interface. These tests become slightly enriched in ^{13}C ($\delta^{13}C$ of ~1 per mil) with regards to the $\delta^{13}C\sum CO_2$ of mean ocean water ($\delta^{13}C$ of ~0 per mil) [Rubinson & Clayton, 1969]. Measuring the $\delta^{13}C$ in the tests of benthic foraminifera of the genus *Cibicidoides* is the ideal method of constructing these records. Species of this genus can be used to reconstruct the $\delta^{13}C\sum CO_2$ of former ocean deep and bottom-water masses [Mackensen et al., 1993; Marchal & Curry, 2008]. Therefore, the resulting $\delta^{13}C$ records can be

used as proxies, indicating past nutrient distributions with implications for ocean circulation and atmospheric CO_2 patterns, particularly during late Quaternary climatic cycles [Mackensen et al., 1993; Oppo & Lehman, 1995; Bickert et al., 1997; Venz et al., 1999; Flower et al., 2000; Poli et al., 2000; Raymo et al., 2004; Ferretti et al., 2005; Lisiecki & Raymo, 2005; Dickson et al., 2008; Hodell et al., 2008; Ferretti et al., 2010; Billups et al., 2011].

One reason why *Cibicidoides* spp. are ideal for deep ocean circulation reconstructions is that they are epifaunal, meaning they live on top of sediment, and secrete their tests from ocean water above the sediment interface. This is important because increased remineralization of organic material below the sediment interface can potentially alter the preformed $\delta^{13}C$ signature of the water mass present. The use of *Cibicidoides* spp. is also ideal for deep water reconstructions because they are widespread throughout all of the deep ocean basins, allowing for data comparison without unnecessary species corrections. One major complication, however, is that in certain core-depths, particularly at Site 1063 during this interval of time, foraminifera of the *Cibicidoides* genus may be rare, absent, or too small to accurately measure the $\delta^{13}C$ in their tests. In these instances, the $\delta^{13}C$ of the infaunal benthic species, *Oridorsalis umbonatus,* may be used to fill the gaps left in the $\delta^{13}C$ record from the absence of *Cibicidoides* (mostly *C. mundulus* at Site 1063), as *O. umbonatus* has been found to be applicable as an additional, robust water mass-tracer [Katz et al., 2003; Billups et al., 2011]. Furthermore, data from *Oridorsalis umbonatus* tests have been used in previously published records of Poli et al. [2000], Ferretti et al. [2005], and Billups et al. [2011] at Site 1063, specifically. Therefore, I saw no problem in using data from *Oridorsalis umbonatus* specimen to fill gaps in my *Cibicidoides* record. However, to do so, a correction of *Oridorsalis umbonatus* to *Cibicidoides mundulus* must be applied for the records to be comparable ($\delta^{18}O$ - 0.59; $\delta^{13}C$ + 1.19 [Billups et al., 2011]) at Site

1063. These two species are particularly useful in creating high resolution records, to best link the previously published records from Site 1063 [Poli et al., 2000; Ferretti et al., 2005; Billups et al., 2011].

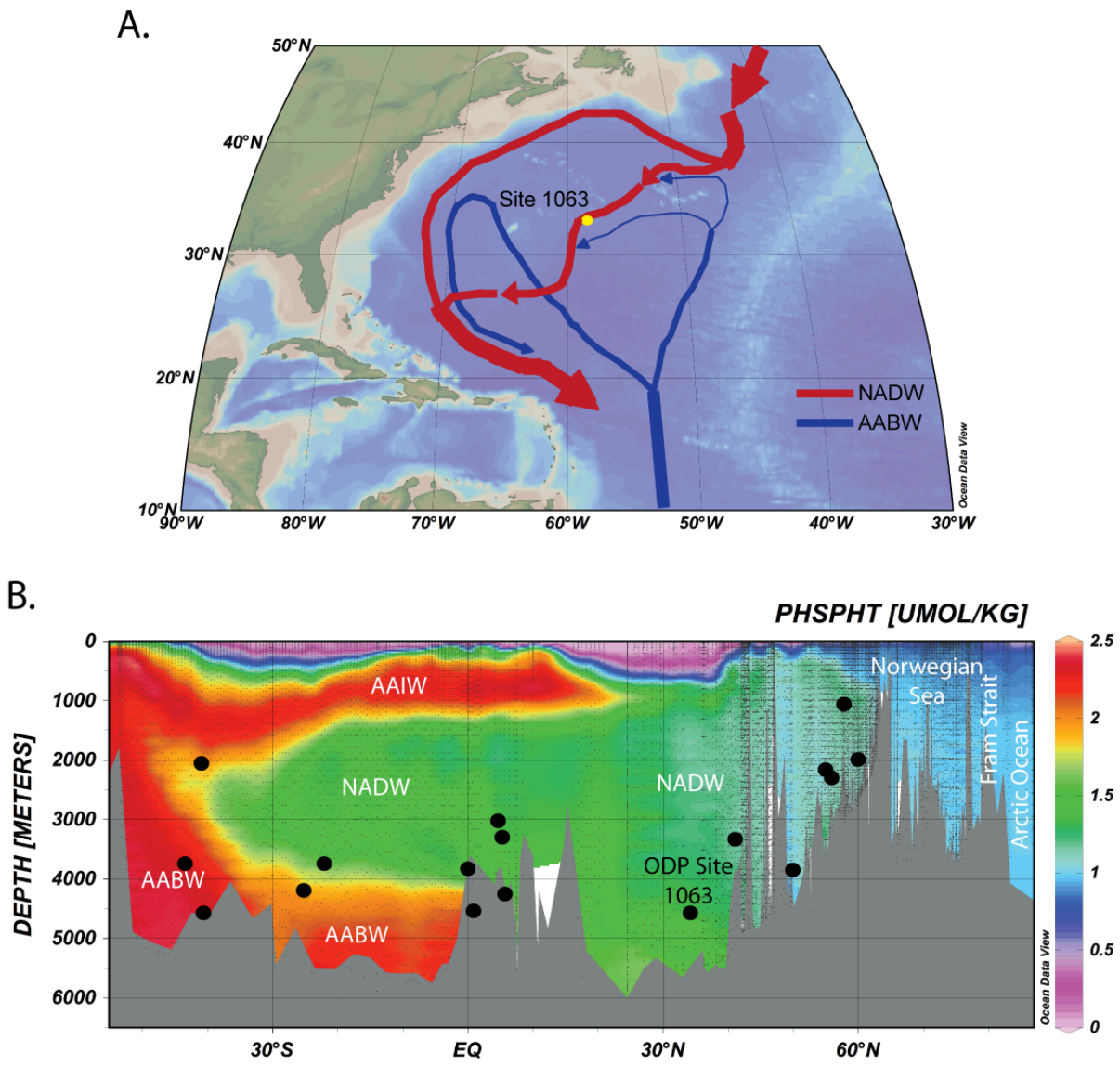

Figure 3.1 **A.** Bathymetric map identifying the location of ODP Site 1063 in relation to the generalized modern deep-water currents of the North Atlantic Deep Water (NADW) and Antarctic Bottom Water (AABW) masses [Hoogakker et al., 2007: after McCave & Tucholke, 1986]. **B.** Cross-sectional view of the distribution of the NADW, AABW, and Antarctic Intermediate Water (AAIW) masses (as indicated by dissolved phosphate concentrations) in the Atlantic Ocean in relation to ODP Site 1063 (34N, 58W, 4583m). Also identified are the locations of sites to which the $\delta^{13}C$ record from Site 1063 will be compared to below (Table 5.1).

Chapter 4

METHODS

4.1 Sample Preparation

This project involved 713 sediment samples (2cm-down-core intervals) from ODP Site 1063 spanning from MIS 13 to MIS 18 (~500 to 750 ka). These samples were taken at 5 cm intervals from 108.36 to 144.09 mcd. Approximately 95% of each sediment sample was dried overnight in a lab-oven at ~50^{o}C, and weighed. Following this initial weighing procedure, each sample was soaked in Calgon (sodium metaphosphate/buffered DI) solution overnight to disaggregate. The sample was then washed through a 63 μm sieve to retain the sand-sized sediment fraction. After air-drying overnight, the remaining sediment was re-weighed to determine the total mass (%) of sand-sized particles within each sample (the remaining ~5% of each sample was archived). From the resulting sediment of the ≥ 63 μm size fraction, all *Cibicidoides* spp. and *Oridorsalis umbonatus* specimen were picked that were ≥ 150 μm in diameter (dry sieved).

4.2 Stable Isotope Analyses

From every possible interval, one or two of the picked benthic foraminiferal specimen were prepared for stable isotope analysis. Specimen were placed in vials and oven dried overnight. These vials were then loaded into a GV Instruments IsoPrime dual inlet stable isotope ratio mass spectrometer equipped with a Multiprep sample preparation system. This instrument dissolves the $CaCO_3$ test of the foraminiferal specimen(s) in dehydrated phosphoric acid:

$$CaCO_3 + H_3PO_4 \rightarrow CaHPO_4 + CO_2 + H_2O \qquad \text{(Eq. 4.1)}$$

Each run on the mass spectrometer contained in-house standards (Carrara Marble), which are used to report the data to VPDB. The analytical precision of the instrument is better than 0.08 per mil for $\delta^{18}O$ and 0.06 per mil for $\delta^{13}C$ in a size range of 20 to 200 μg.

To test the species correction of Billups et al. [2011] on this time interval, a total of 44 samples had duplicate stable isotope analyses conducted on both *Cibicidoides mundulus* and *Oridorsalis umbunatus* specimen. From these samples, I calculated an offset correction of $\delta^{18}O_{Or} - 0.71$ (standard deviation of 0.36 per mil) and $\delta^{13}C_{Or} + 1.24$ (standard deviation of 0.53). The difference between this offset and that calculated by Billups et al. [2011] is statistically insignificant, and close to the analytical precision range for the instrument. Therefore, in order to best link the various data sets, I applied the published species correction of *O. umbunatus* to *C. mundulus* of Billups et al. [2011] from Site 1063 ($\delta^{18}O - 0.59$; $\delta^{13}C + 1.19$). After applying this correction to the stable isotope data from all *Oridorsalis umbunatus* specimen, the spliced data from both species created a relatively smooth time series (Figure 4.1).

In order to construct the highest resolution record possible, I sent a total of 108 samples (76 *C. mundulus*; 32 *O. umbunatus*) to the University of South Carolina (USC) as our mass spec was down for an extended period of time. To identify and correct for potential laboratory offsets, I also sent samples of our in-house standard, Carrara Marble. The $\delta^{18}O$ and $\delta^{13}C$ values of the standard were comparable indicating no apparent offsets between the two laboratories. However, it became clear that the $\delta^{18}O$ values for the benthic foraminiferal samples analyzed at USC are significantly lower than duplicate values analyzed at UD (-0.45 per mil) whereas offsets

in the $\delta^{13}C$ values are small (+0.13 per mil) (Figure 4.2A). As no differences in values were found in the Carrara Marble standards, which have much lower values than typical benthic foraminifera ($\delta^{18}O$: -1.91 per mil versus 3-4 per mil; $\delta^{13}C$: 2.07 per mil versus 0-1 per mil, respectively), this discrepancy cannot be explained by commonly observed laboratory offsets (e.g., Ostermann & Curry [2000]). More likely it is due to a non-linearity associated with the isotopic composition of the sample arising when the sample-standard values are not similar. As the USC values match well with values that were generated at UD before the instrument went down, the problem is with our mass spectrometer at UD. The causes of this non-linearity are still under investigation. However, it is possible to use the eleven duplicate samples to correct the UD data set ($\delta^{18}O_{UD} - 0.45$, $\delta^{13}C_{UD} + 0.14$). This correction produced excellent agreement between the two data sets (Figure 4.2B).

After applying all of the necessary corrections applied above, I constructed the complete stable isotope records by using all of the available *C. mundulus* data (duplicate values averaged), and *O. umbunatus* data to fill any gaps to the extent possible (duplicate values averaged). I then removed all obvious outliers, identified by being outside two standard deviations of a local five point moving average. This ultimately resulted in a complete $\delta^{18}O$ record of 340 data points, and a complete $\delta^{13}C$ record of 339 data points, between MIS 13 and MIS 18.

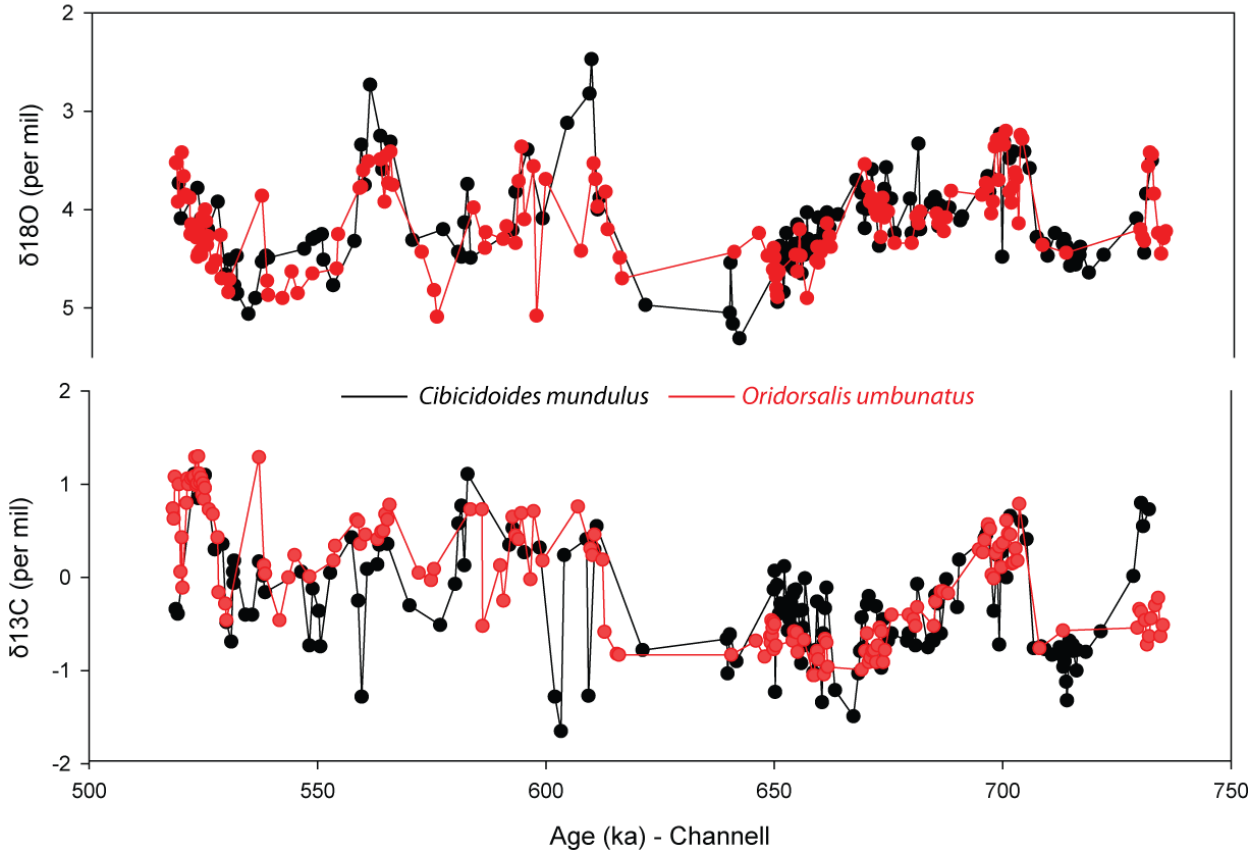

Figure 4.1: Agreement between stable isotope data from the two benthic foraminiferal species after applying the species correction of Billups et al. [2011] of *Oridorsalis umbunatus* to *Cibicidoides mundulus* of $\delta^{18}O_{Or.} - 0.59$ and $\delta^{13}C_{Or.} + 1.19$.

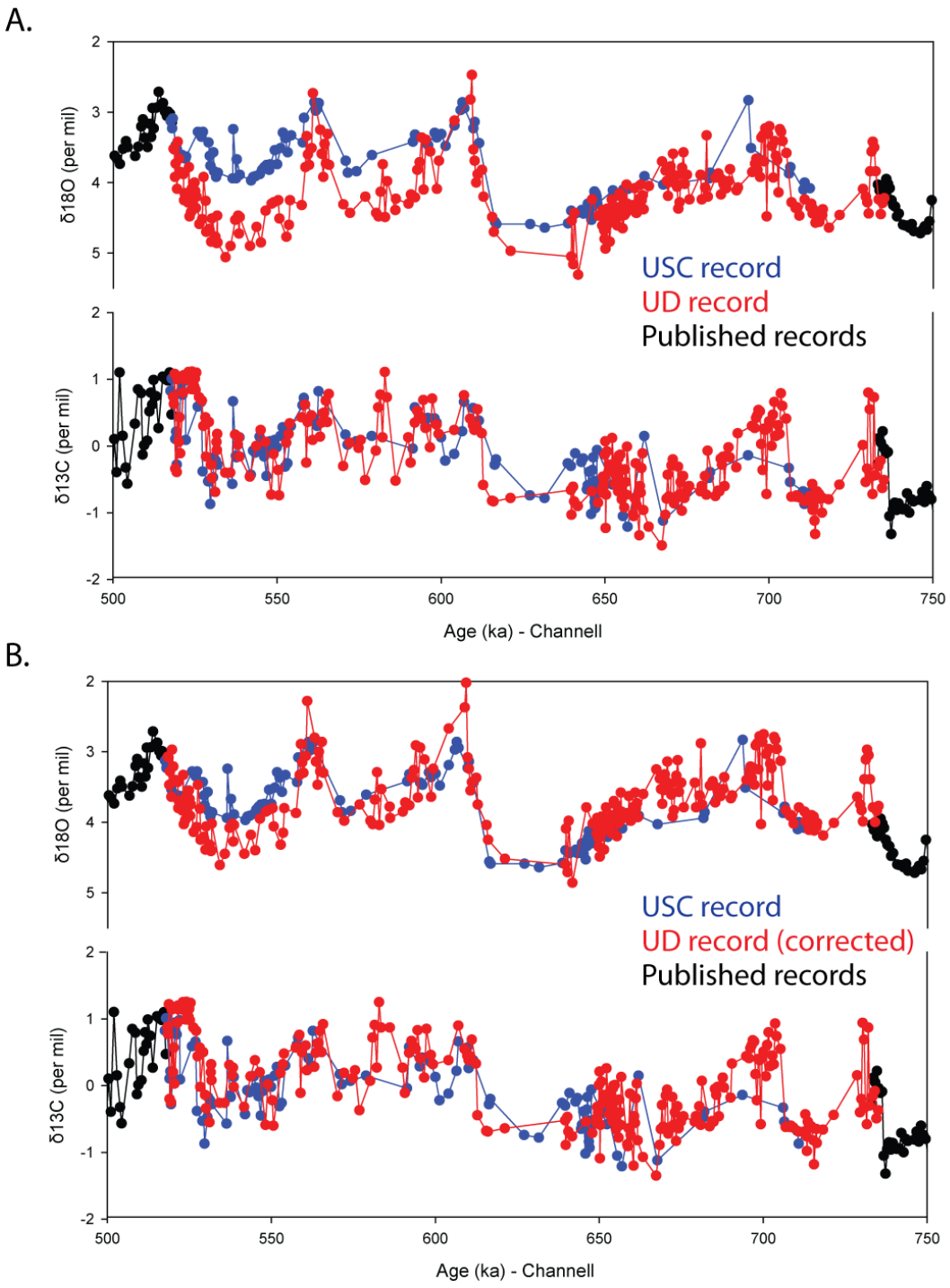

Figure 4.2: The stable isotope data for this study generated from the University of Delaware (UD) mass spectrometer (red), and the University of South Carolina (USC) mass spectrometer, in relation to the previously published records before and after this study interval (black). The raw data **A.** shows an offset between the UD and USC-generated records, compared to **B.** the better agreement of the data after applying the offset correction of $\delta^{18}O_{UD} - 0.45$ and $\delta^{13}C_{UD.} + 0.14$. Outliers were identified (outside two standard deviations with respect to a five point moving average) and removed prior to the construction of this figure to better demonstrate the agreement following this correction.

Chapter 5

AGE MODEL DEVELOPMENT

5.1 Preliminary Age Model

The stable isotope data presented below were placed on the preliminary age model of Channell et al. [2012], which revised the original age model for ODP Site 1063 of Grutzner et al. [2002]. The age model of Channell et al. [2012] was determined by tandem correlation of planktonic oxygen isotope (MIS 1 through MIS 24) and relative paleointensity data to calibrated reference templates from ODP Site 1063. This revisited chronology applied the most recently established ages of various magnetic excursions to the full planktic foraminiferal record. The resulting planktic oxygen isotope record on the Channell et al. [2012] age model was in better agreement with the LR04 global stack of Lisiecki & Raymo [2005] than that on the Grutzner et al. [2002] age model. Applying this revisited paleointensity-derived age model to my benthic stable isotope records from MIS 13 to MIS 18 was adequate to compare my results to those previously published at Site 1063 (*see section 6.1*). However, in order to compare the Site 1063 composite record (*see section 6.2*) to others throughout the Atlantic Ocean, a common age model was needed.

5.2 Age Tuning to LR04 Global Stack

In order to be able to compare the full composite stable isotope record (*see section 6.3*) from Site 1063 to others published throughout the Atlantic Ocean (Table 5.1), it was necessary to normalize them to a common age model. Therefore, I tuned the full composite $\delta^{18}O$ record from

Site 1063 to the LR04 global benthic $\delta^{18}O$ stack of Lisiecki & Raymo [2005]. This was accomplished by using the AnalySeries software package to tune distinct $\delta^{18}O$ features from the Site 1063 record to those corresponding in the LR04 stack (Figure 5.1A). From this tuning, the full composite $\delta^{18}O$ record from Site 1063 corresponds to the time interval from ~250 to 1030 ka (Figure 5.1).

5.3 Tuned Age Model Analysis

To get a sense of the quality of agreement between the LR04 stack [Lisiecki & Raymo, 2005] and the composite Site 1063 records, band-pass filters at the obliquity (41-kyr) and precession (23-kyr) periodicities were applied. These filters were applied with frequency/bandwidths of 0.025/0.006 and 0.045/0.01, respectively, and reveal good first-order agreement resulting from their tuning (Figure 5.1B). Additionally, cross-spectral analyses between the two records were conducted to ensure confidence in the tuning strategy and to quantify the agreement between them (Figure 5.2). This utilized the Crosspec program from the Arand software package available online at http://www.ncdc.noaa.gov/paleo/softlib/arand/arand.html. Both records were linearly detrended and re-assigned a 1,500-yr timestep, which adequately captures the major orbital bands. The cross-spectral analysis ran with 519 data points and used 175 lags. The resulting coherencies were very high at the ~100-kyr (0.984), ~41-kyr (0.990), and ~23-kyr (0.963) periods, well above the test statistic for non-zero coherency at 95% confidence of 0.798 (Figure 5.2). Furthermore, after tuning the full Site 1063 record to the LR04 stack, both records are in phase at each of these major orbital periods (Figure 5.2).

Program	Core	Location	Lat (°N)	Long (°E)	WD (m)	Source
ODP	552	N.A.	56.485	-23.231	2301	Raymo et al., 1997
ODP	607	N.A.	41.000	-33.000	3427	Raymo et al., 1997
ODP	980	N.A.	55.485	-14.702	2168	Flower et al., 2000
ODP	982	N.A.	57.513	-15.875	1145	Venz & Hodell, 1999
ODP	983	N.A.	60.000	-24.000	1983	Raymo et al., 1997
U	1308	N.A.	50.000	-24.000	3871	Hodell et al., 2008
ODP	**1063**	**sub N.A.**	**34.000**	**-58.000**	**4583**	**Poli et al., 2000; Ferretti et al., 2005; Billups et al.,**
ODP	664	E.N.A.	0.100	-23.233	3806	Raymo et al., 1997
ODP	925	E.N.A.	4.203	-43.489	3040	Bickert et al., 1997
ODP	927	E.N.A.	5.462	-44.480	3326	Bickert et al., 1997
ODP	929	E.N.A.	5.977	-43.740	4369	Bickert et al., 1997
GeoB	1101	E.N.A.	1.658	-10.980	4588	Bickert et al., 2003
RC13	229	S.A.	-25.490	11.307	4191	Oppo et al., 1990
GeoB	1034	S.A.	-21.735	5.422	3772	Bickert et al., 2003
ODP	1088	S.A.	-41.137	13.563	2082	Hodell et al., 2000
ODP	1089	S.A.	-40.937	9.893	4621	Hodell et al., 2000
ODP	1090	S.A.	-42.913	8.898	3700	Becquey & Gersonde, 2002

Table 5.1: Table identifying the site, regional location (North Atlantic – N.A.; Equatorial North Atlantic – E.N.A., South Atlantic – S.A.), latitude, longitude, water depth, and reference information for the 16 stable isotope records to which the composite record from ODP Site 1063 will be compared. To see their distribution throughout the deep Atlantic Ocean in relation to the modern water mass distribution, see Figure 3.1B.

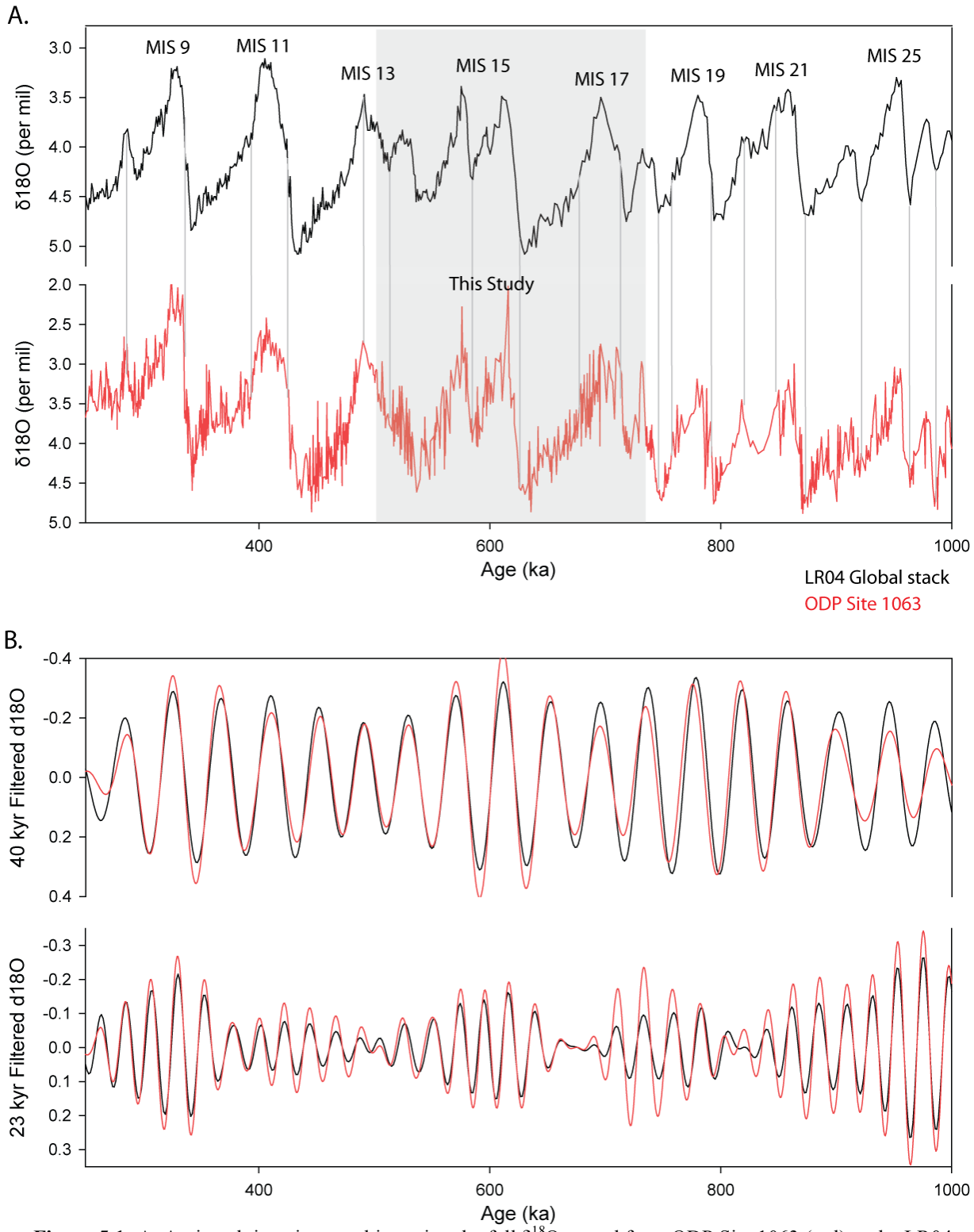

Figure 5.1: A. Assigned tie points used in tuning the full $\delta^{18}O$ record from ODP Site 1063 (red) to the LR04 global benthic $\delta^{18}O$ stack [Lisiecki & Raymo, 2005]. **B.** Band pass filters at the obliquity and precession periods show good agreement between the two records.

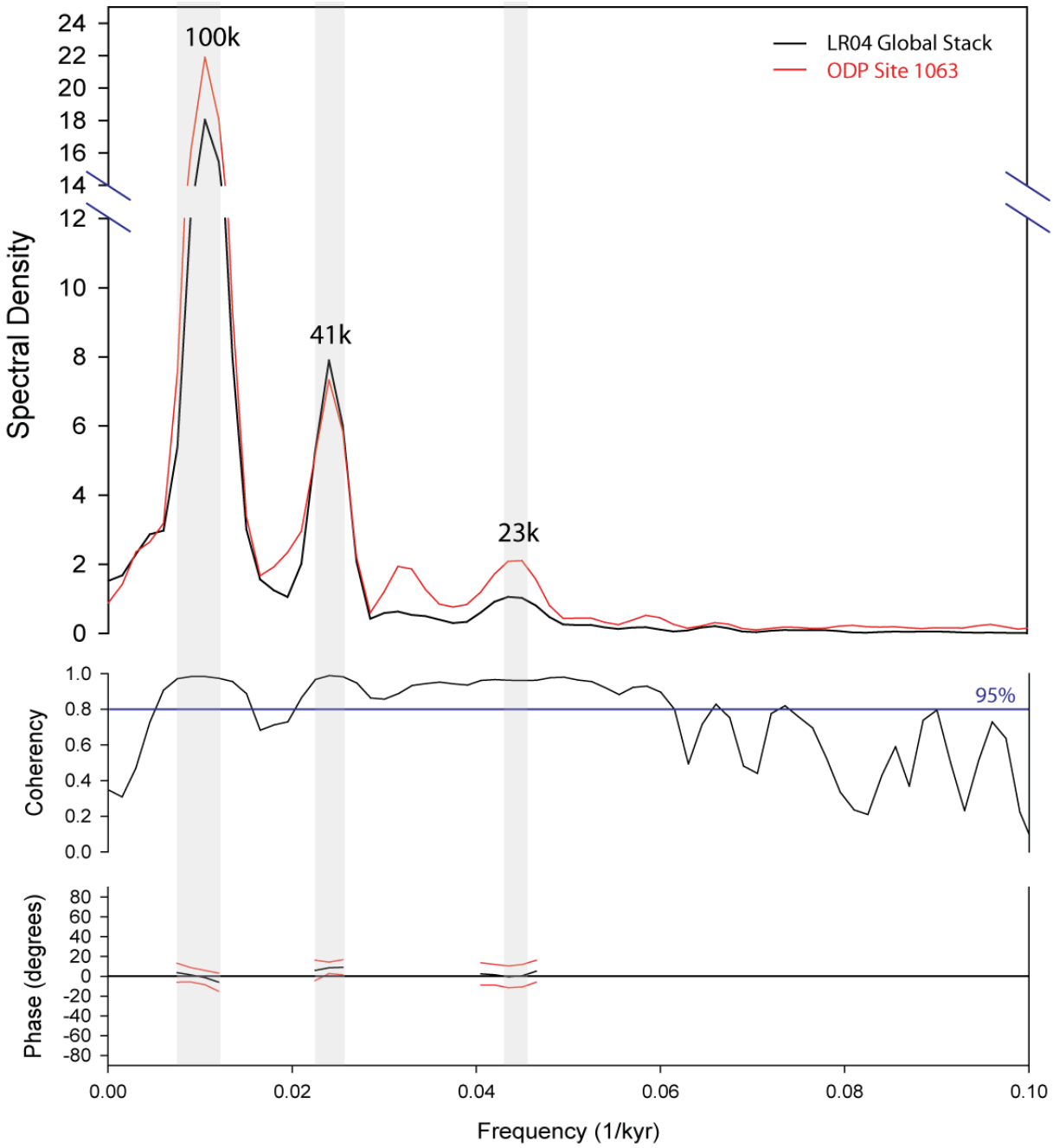

Figure 5.2: Results from cross-spectral analysis between the LR04 global benthic $\delta^{18}O$ stack [Lisiecki & Raymo, 2005] and the tuned full Site 1063 $\delta^{18}O$ record to quantify the quality of the tuning. Spectral peaks in all three major orbital periodicities are in agreement, highly coherent, and in phase with one another.

Chapter 6

RESULTS

6.1 ODP Site 1063: MIS 13 to MIS 18

The stable isotope records constructed here range from MIS 13 (~500ka) to MIS 18 (~740ka – Figure 6.1). Interglacial periods MIS 13, MIS 15, and MIS 17 are identified by low $\delta^{18}O$ values (~3 per mil – Figure 6.1A), and high $\delta^{13}C$ values (~0.5 to 1 per mil – Figure 6.1B). Alternatively, glacial periods MIS 14, and MIS 16 are characterized by relatively high $\delta^{18}O$ values (~4.5 per mil) and low $\delta^{13}C$ values (~ -0.5 to -1 per mil – Figure 6.1). A negative $\delta^{18}O$ excursion (to ~3 per mil) occurred during the MIS 18 glacial period, with a corresponding positive $\delta^{13}C$ excursion (to ~1 per mil – Figure 6.1). While appearing out of place for a glacial period, this event within MIS 18 is common throughout the global ocean, evident by its presence in the LR04 global stack (Figure 2.1) [Lisiecki & Raymo, 2005]. Overall, these $\delta^{18}O$ and $\delta^{13}C$ values are comparable to the younger portion of the record produced by Poli et al. [2000] and Billups et al. [2011] during both glacial and interglacial periods (Figure 2.3). However, the $\delta^{18}O$ and $\delta^{13}C$ values presented here during interglacial periods MIS 13, MIS 15, and MIS 17, are more negative and positive, respectively, than the $\delta^{18}O$ and $\delta^{13}C$ values from the older section of the Site 1063 record (Figure 2.3) [Ferretti et al., 2005].

When comparing these records to others from sites throughout the deep-Atlantic Ocean, several trends were noticed. During the glacial periods MIS 14, MIS 16, and MIS 18, the $\delta^{13}C$ values recorded at the site overlap with those recorded from South Atlantic sites ODP Site 1089 [Hodell et al., 2000] and Site 1090 [Becquey & Gersonde, 2002] (Figure 6.1B). Alternatively,

the $\delta^{13}C$ values during the MIS 13, MIS 15, and MIS 17 interglacial periods are similar to values from the North Atlantic ODP Site 980 [Flower et al. 2000] and Site 607 [Raymo et al. 1997] (Figure 6.1C). Overall, these results are consistent with the observations discussed above from the published records of Poli et al. [2000] and Billups et al. [2011] with more negative $\delta^{13}C$ values during glacial periods (similar to southern-sourced sites – Figure 6.1B) and more positive $\delta^{13}C$ values during interglacial periods (similar to northern-sourced sites – Figure 6.1C). It is important to note that despite $\delta^{13}C$ values similar to northern sites during interglacial periods and southern sites during glacial periods on average, $\delta^{13}C$ fluctuations between the two end members persist throughout the entire record on millennial timescales (Figure 6.1).

6.2 Composite Record (MIS 8 to MIS 29)

By combining the stable isotope records from Site 1063 of Poli et al. [2000], Ferretti et al. [2005], and Billups et al. [2011] with those constructed here, the full composite record from Site 1063 spanned from MIS 8 to MIS 29 (~250 to 1030 ka – Figure 6.2). This record contains ten full glacial-interglacial cycles affording a long-term view of the evolution of stable isotope records during the MPT. Throughout this record, $\delta^{18}O$ maxima occurred during glacial periods ranging from ~4.7 to 3.5 per mil, and $\delta^{18}O$ minima during interglacial periods were ~3.2 per mil prior to MIS 17, and between ~2.8 and 2 per mil after MIS 17 (MIS 15, MIS 13, MIS 11, MIS 9) (Figure 6.2A). The $\delta^{18}O$ record reveals the first examples of the asymmetric "saw-tooth" shape typical of late Pleistocene glacial cycles from MIS 25 to MIS 22 and from MIS 17 to MIS 16 (Figure 6.2A).

Similar to the more pronounced interglacial maxima found in the $\delta^{18}O$ record, the $\delta^{13}C$ data identify change beginning at the onset of MIS 17. Prior to MIS 17, $\delta^{13}C$ maximum values

of ~0 per mil during interglacial periods and minimum values of -1 to -1.5 per mil during glacial periods are nearly identical to ODP Site 1089 and Site 1090 from the deep-South Atlantic (Figure 6.2B). This holds true for the glacial periods throughout the entire record, but beginning with the onset of the MIS 17, interglacial $\delta^{13}C$ values of ~0.5 to 1 per mil persist, which are more similar to those from sites in the North Atlantic (Figure 6.2C). These results imply a changing influence of northern vs. southern water mass signatures at Site 1063 within the MIS 13 to MIS 18 time period (~500 to 750 ka). This suggests that a distinct change in deep water circulation changes occurred at Site 1063 during the MPT, at least ~300-kyr prior to the timing of NADW enhancement inferred from the shallower ODP Site 607 [Raymo et al., 1997], located within the less sensitive core of NADW. Overall, the results from the Site 1063 stable isotope records support my hypothesis that changes in deep ocean circulation were more closely linked to reorganization of the climate system during the MPT than previously thought.

6.3 Cross-spectral Analyses between $\delta^{18}O$ & $\delta^{13}C$

To assess the relationship between deep-water circulation and ice volume at Site 1063 at orbital time-scales, cross spectral analysis were conducted between the $\delta^{18}O$ and $\delta^{13}C$ values of the composite record. This was conducted using the Crosspec program from the Arand software package available online at http://www.ncdc.noaa.gov/paleo/softlib/arand/arand.html. Following the same setup as the cross spectral analysis conducted for the tuned age model, both records were linearly detrended and re-assigned a 1,500-yr timestep, which adequately captures the major orbital bands. The cross-spectral analysis therefore ran with 519 data points, and I assigned it to use 175 lags. Spectral peaks at the 100k, 41k, and 23k periods were significant, and highly coherent with one another (greater than the test statistic for non-zero coherency at

95% confidence – Figure 6.3). The lack of coherent spectral peaks in the19-kyr precession band is commonly found in various previously published records spanning this interval of time [Mix et al. 1995a, 1995b; Lisiecki & Raymo, 2008].

Information on phase of $\delta^{13}C$ relative to $\delta^{18}O$ is meaningful where there are significant shared (coherent) spectral peaks [Mix et al. 1995b]. At the 100k frequency, $\delta^{13}C$ appears to either be in phase, or to slightly lead $\delta^{18}O$ ($-10^{o} \pm 10^{o}$) (Figure 6.3). The $\delta^{13}C$ record is in phase with $\delta^{18}O$ at the 41-k frequency ($-7^{o} \pm 17^{o}$), and $\delta^{13}C$ lags $\delta^{18}O$ at the 23-kyr frequency ($37^{o} \pm 18^{o}$) (Figure 6.3). A slight lead of $\delta^{13}C$ relative to $\delta^{18}O$ at the 100-kyr period is consistent with deep sites in the Pacific Ocean, thought to record the mean ocean isotopic values throughout the Pleistocene [Mix et al. 1995a, 1995b]. The result of $\delta^{13}C$ being in phase with $\delta^{18}O$ at obliquity, and lagging $\delta^{18}O$ in precession is consistent with other deep-Atlantic sites [Flower et al., 2000; Lisiecki & Raymo, 2008]. These results suggest that deep circulation and ice volume changes are coupled at the 41-kyr period, while a delayed response of the biosphere to precession forcing is likely responsible for the lag $\delta^{13}C$ to ice volume changes at the 23-kyr period [Mix et al., 1995b].

With such a noticeable change in both the $\delta^{18}O$ and $\delta^{13}C$ records beginning around the onset of MIS 17 (Figure 6.3), I wanted to determine whether or not any change in the phase response to orbital forcing occurred at that time. To accomplish this, I ran additional cross-spectral analyses on the composite ODP Site 1063 records in two separate time slices: following (250 to 700 ka – Figure 6.4A) and preceding (700 to 1000 ka – Figure 6.4B) MIS 17. Both of these records were assigned the same 1,500-yr timestep, and given 100 lags (n=219, n=300, respectively). These analyses did not show any change in the phase relationship at any of the major orbital bands (Figure 6.4). From this I deduce that no noticeable change in response to

orbital forcing coincides with the transition found within Site 1063's stable isotope records at the onset of MIS 17. The change in deep water circulation is likely a response to a unique series of events in the source region of NADW formation, which is the focus of Chapter 7.

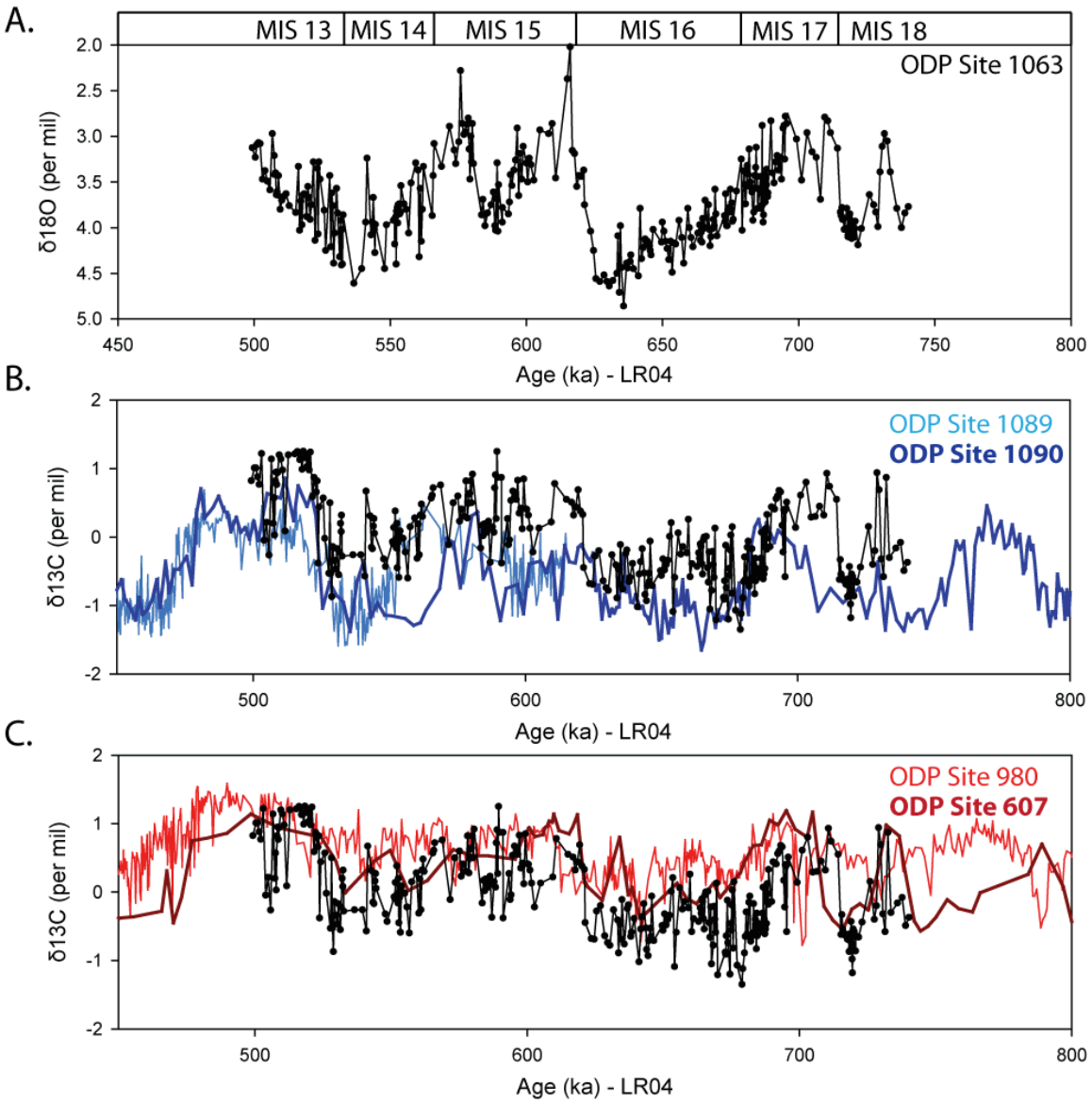

Figure 6.1: **A.** The $\delta^{18}O$ record produced in this study with MIS 13, MIS 14, MIS 15, MIS 16, MIS 17, and MIS 18 identified. The $\delta^{13}C$ record constructed within this study is shown in relation to **B.** to the $\delta^{13}C$ records from ODP Site 1089 (4621m [Hodell et al., 2000]) and ODP Site 1090 (3700m [Becquey & Gersonde, 2002]) in the deep South Atlantic source region of AABW, and **C.** to the $\delta^{13}C$ records of ODP Site 980 (2168m [Flower et al., 2000] and ODP Site 607 (3427m [Raymo et al., 1990; 1997] from the deep North Atlantic source region of NADW.

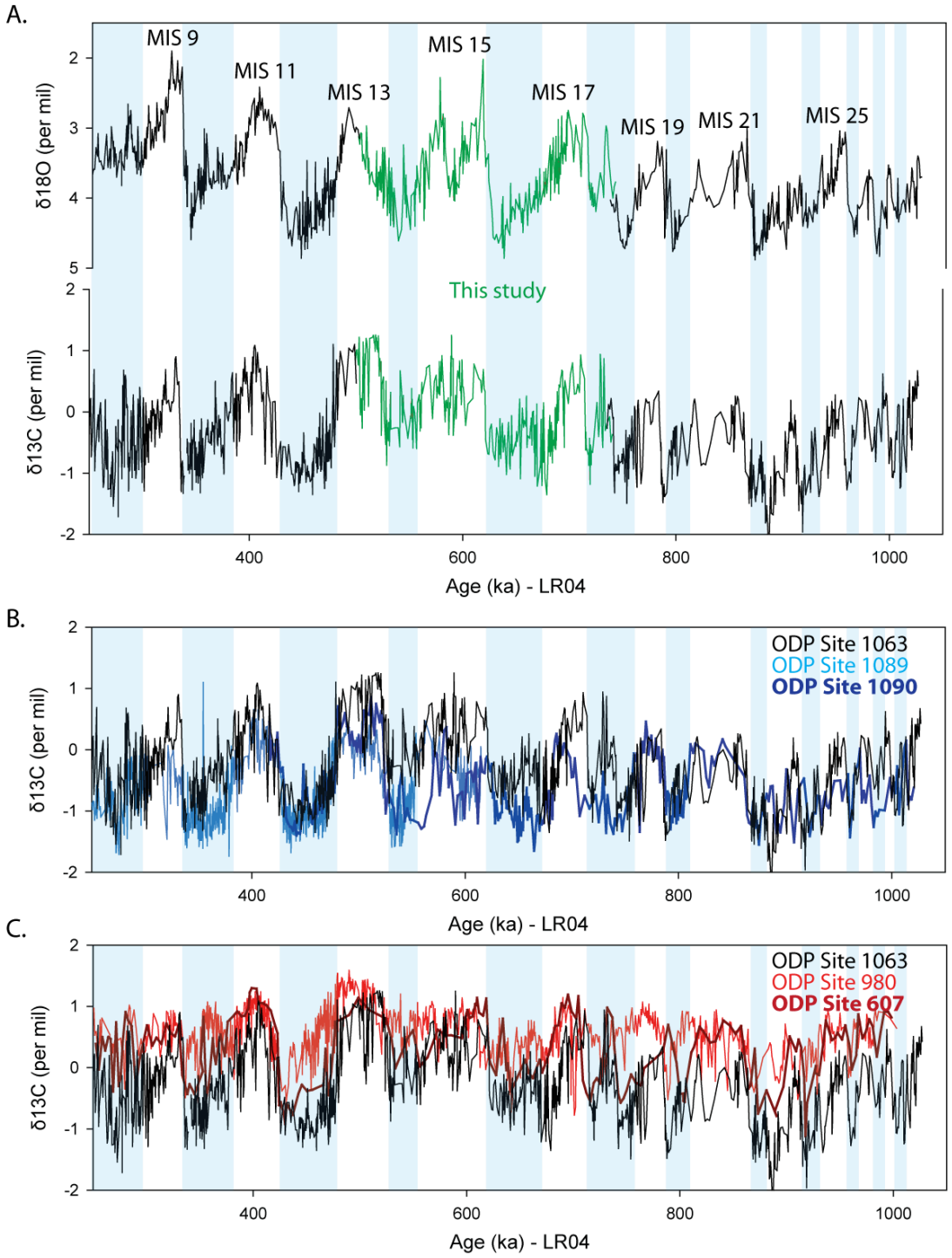

Figure 6.2: **A.** The complete composite $\delta^{18}O$ and $\delta^{13}C$ record produced in this study, with the interglacial periods identified. The $\delta^{13}C$ record constructed within this study is shown in relation to **B.** to the $\delta^{13}C$ records from ODP Site 1089 (4621m [Hodell et al., 2000]) and ODP Site 1090 (3700m [Becquey & Gersonde, 2002]) in the deep South Atlantic source region of AABW, and **C.** to the $\delta^{13}C$ records of ODP Site 980 (2168m [Flower et al., 2000] and ODP Site 607 (3427m [Raymo et al., 1990; 1997] from the deep North Atlantic source region of NADW.

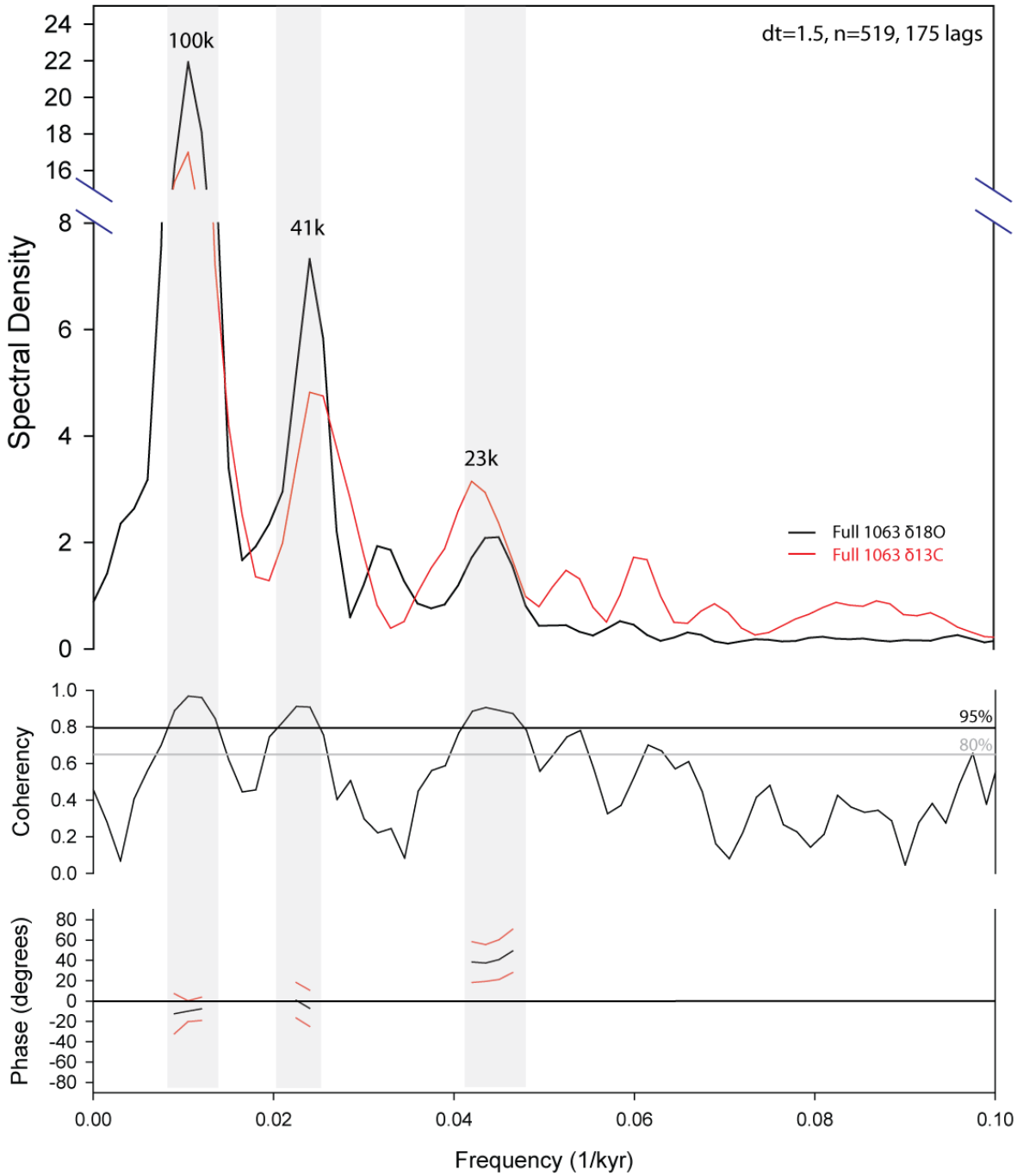

Figure 6.3: Cross-spectral results between the composite $\delta^{18}O$ and $\delta^{13}C$ records from Site 1063 with coherent (to 95% confidence) spectral peaks at all three major orbital periods (100k, 41k, 23k). Phase relationships between the two records are also shown at these orbital periods, with positive phase representing a $\delta^{18}O$ lead of $\delta^{13}C$, and inversely a negative phase representing a $\delta^{13}C$ lead of $\delta^{18}O$.

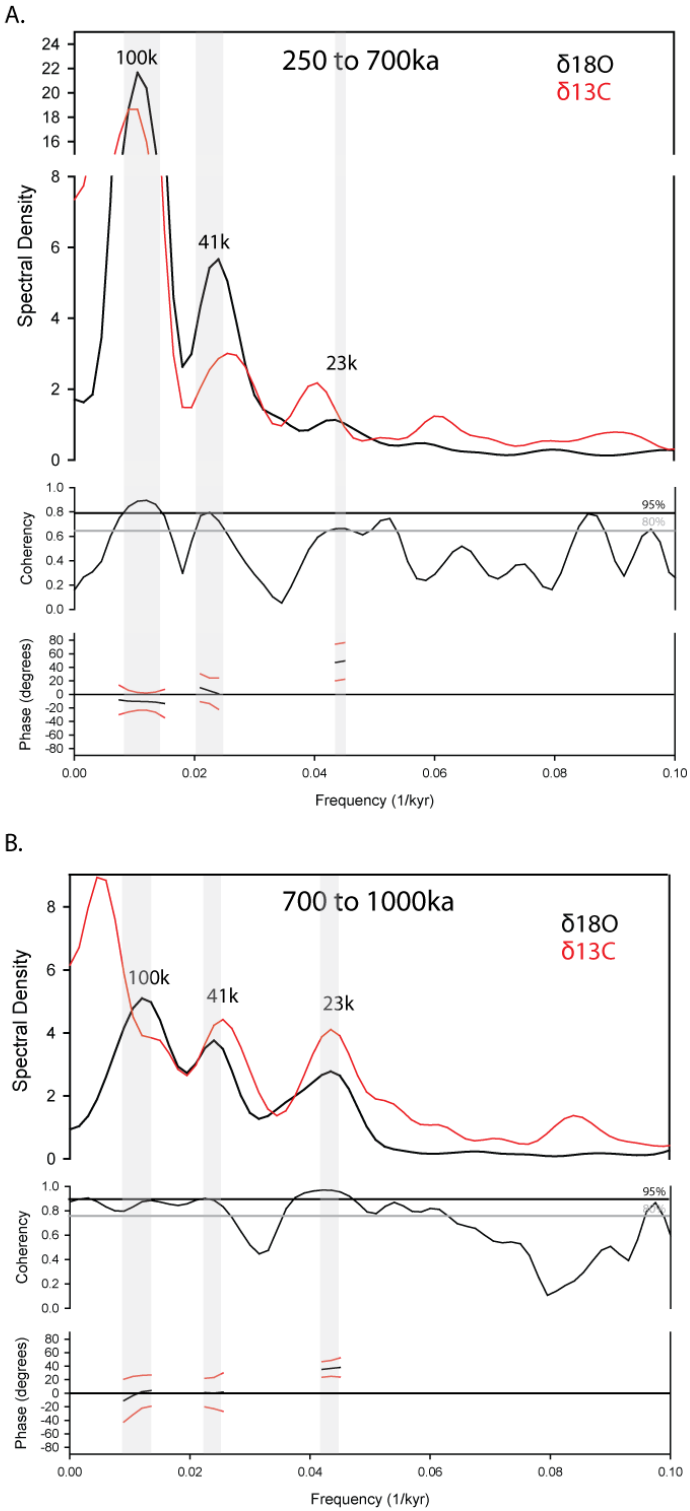

Figure 6.4: Cross-spectral results between the $\delta^{18}O$ and $\delta^{13}C$ records from Site 1063 separated into two time periods: **A.** from ~250 to 700ka (after MIS 17), and **B.** from ~700 to 1000ka (before MIS 17). These two time slices both exhibit coherent spectral peaks, with consistent phase relationships between $\delta^{18}O$ and $\delta^{13}C$, at the 100k, 41k, and 23k periods.

Chapter 7

DISCUSSION

7.1 Intensification of NADW Influence at ODP Site 1063

The ODP Site 1063 $\delta^{13}C$ record indicates that over the time interval from ~750 to 500ka, a shift in deep-water influence occurred in the deepest region of the North Atlantic Ocean, supporting a link with the MPT. Specifically, my results show that this change occurred at the onset of MIS 17 (Figure 6.2). Based on the findings that from ~1Ma to 700ka of the composite Site 1063 record (MIS 29 to MIS 18), glacial and interglacial $\delta^{13}C$ values at the site correspond to sites from the deep-South Atlantic (Figure 6.2B), I determined that the deep North Atlantic Ocean was under the primary influence of AABW below 4500m. While AABW influence during glacial periods continued throughout the entire record (Figure 6.2B), NADW began to influence the deepest North Atlantic during the beginning of the MIS 17 interglacial period (Figure 6.2C). The shift at Site 1063 from southern-sourced $\delta^{13}C$ values during MIS 18 to northern-sourced $\delta^{13}C$ values throughout MIS 17 suggests an abrupt NADW-enhancement during glacial termination. The fact that this strong NADW influence continued at Site 1063 at the initial onset of each of the following interglacial periods thereafter, in conjunction with the evolution of the "saw-tooth" shaped glacial cycles, suggests that a change in the response at glacial termination occurred during the MPT. The onset of this NADW enhancement at ODP Site 1063 occurred ~300-kyr prior to the establishment of more extreme interglacial periods at ~400ka, starting with MIS 11.

7.2 Geospatial Extent of NADW-enhancement

In order to determine whether these changes in deep-water mass influence/distribution were local or evident throughout the entire Atlantic Ocean, I compared the ODP Site 1063 $\delta^{13}C$ record to 16 previously published $\delta^{13}C$ records from the North, Equatorial, and South Atlantic Oceans (Figure 3.1; Table 5.1). From these various sites, average $\delta^{13}C$ values corresponding to interglacial maxima ($\delta^{18}O$ minima) for each interglacial period (MIS 9, MIS 11, MIS 13, MIS 15, MIS 17, MIS 19, MIS 21, MIS 25, MIS 27, MIS 29) were imported into the Ocean Data View (ODV) program (Table 7.1) [Schlitzer, 2012]. From these data, I constructed cross sections of $\delta^{13}C$ gradients along transects from 60°N to 60°S, corresponding to the location of the published sites (Figure 7.1). These $\delta^{13}C$ gradients were constructed by interpolating between data points from each site via the "DIVA-gridding" option [Schlitzer, 2012]. In order to interpret this data, I must assume that these average $\delta^{13}C$ values during interglacial maxima ($\delta^{18}O$ minima) provide a snapshot of the average interglacial conditions at each site, and that the interpolated gridding between data points provides a good first-order estimate for the likely extent of deep-water masses. Keeping these assumptions in mind, the resulting snap shot approximations of deep-water mass extent throughout the Atlantic Ocean appear to be consistent with the results from the composite record of ODP Site 1063. They reveal an increasing influence of interglacial-NADW in the North Atlantic first during MIS 19 (depths of ~2000 to 4000m), which then propagated to depths greater than ~4500m during the MIS 17 interglacial period (Figure 7.1). The fact that production of this dense, lower limb of NADW appears to remain strong in the deep North Atlantic during each of the following interglacial periods (MIS 15, MIS 13, MIS 11, and MIS 9) is also consistent with the results discussed from the Site 1063 record (Figure 7.1).

7.3 Enhancement of Interglacial-NADW Production during the MPT

By comparing the Site 1063 record with others throughout the deep Atlantic Ocean, it appears as though interglacial production of NADW was relatively weak from MIS 29 through MIS 21 (Figure 7.1). Higher $\delta^{13}C$ values at sites between 2000 and 4000m during the MIS 19 interglacial period suggest a relative increase in the NADW production during this time (Table 7.1; Figure 7.1). Beginning in the MIS 17 interglacial period, production of the densest limb of NADW increased, along with further enhancement of core-NADW production (Figure 7.1). This enhanced NADW production began at Site 1063 simultaneously with the abrupt termination from the MIS 18 glacial period (Figure 6.2C), and persisted throughout most of the MIS 17 interglacial maximum (Figure 6.2C). These trends continued during each of the interglacial periods following thereafter (MIS 15, MIS 13, MIS 11, MIS 9) (Figure 6.2C). These results suggest a progressive intensification of interglacial NADW formation between MIS 19 and MIS 17, from the weaker interglacial NADW formation beforehand.

This change in deep water circulation could possibly be explained by a shift in location of NADW formation. In fact, Denton et al. [2000] proposed that an uplift of the Greenland-Scotland Ridge could have shifted the region of NADW production from the Arctic Ocean to the Norwegian Greenland Sea (NGS), responsible for driving the MPT. However, a recent study by Haley et al. [2008] found that intermediate/deep circulation in the Arctic Ocean was largely unchanged after ~2Ma, when the interglacial circulation regime became similar to the 'pre-anthropocene' circulation in the modern interglacial period [Haley & Polyak, 2013]. Therefore, the enhancement of deep-limb NADW production found here cannot be explained by a shift in

the formation region from the Arctic Ocean to the North Atlantic and NGS during this time period.

Having ruled out the possibility of a shift in location of NADW formation, the intensification of conditions driving NADW formation in the region where it forms today is more likely to explain the findings of this study. The NGS is currently where convection of Atlantic-sourced surface waters feed the densest limb of NADW, along with an addition of deep waters exiting the Arctic Ocean through the Fram Strait [Aagaard et al., 1991; Dickson & Brown, 1994; Bonisch & Schlosser, 1995]. Within the NGS, the Arctic Front (AF) refers to the complex zone of mixing between cold surface waters from the Arctic and the warmer, more saline surface waters derived from the North Atlantic Current (NAC) [Swift & Aagaard, 1981; Johannessen et al., 1994]. The water west of the AF is seasonally covered by sea-ice, promoting relatively weak deep-water convection via brine rejection during winter months [Swift, 1986]. More rigorous deep-water convection occurs to the east of the AF, where the open ocean loss of heat from the saline Atlantic-sourced surface waters occurs during winter months [Schmitz & McCartney, 1993].

A recent study by Alonso-Garcia et al. [2011a] used planktic foraminifer faunal assemblages, along with benthic stable isotope data from sites in the North Atlantic to infer the location of the AF between MIS 19 and MIS 11 (~800 to 400ka) (Figure 7.2). The location of the AF has changed relative to various stages of the low-frequency glacial cycles of the late Pleistocene, with associated changes in NADW production [Alonso-Garcia et al., 2011a]. The orientation of the AF throughout Interglacial periods between MIS 19 and MIS 11 was very consistent [Alonso-Garcia et al., 2011a]. During the early interglacial phase, the AF location was likely comparable to today, indicating inflow of the NAC into the eastern-NGS, where these

saline surface waters cooled and were entrained, generating NADW (Figure 7.2A) [Alonso-Garcia et al., 2011a]. Throughout the late interglacial period, the AF gradually moved southeastwards, enhancing sea ice growth and export [Alonso-Garcia et al., 2011a]. However, continental ice sheets were still waning, and the eastern North Atlantic remained warm due to continued influence of the NAC, and NADW formation in the NGS was strong (Figure 7.2B) [Alonso-Garcia et al., 2011a].

In contrast to relatively stable AF orientation during the early and late phases of interglacial periods characterized by low ice volume, the onset of ice sheet growth had a more pronounced influence on the location of the AF. With the initiation of the growth of ice sheets during the first phase of glacial periods, NAC-derived surface waters still entered the eastern-most NGS, resulting in continued NADW production, while Arctic waters expanded in the western sub-polar North Atlantic dampening Labrador Sea deep-water convection (Figure 7.2C) [Born et al., 2010; Alonso-Garcia et al., 2011a]. During the second phase of glacial periods, the position of the AF fluctuated from positions similar to the late interglacial phase during warm periods, to south of Iceland as a result of calving and meltwater discharges (Figure 7.2D) [Alonso-Garcia et al., 2011a]. This calving and associated ice rafting caused strong reduction of the Atlantic Meridional Overturning Circulation (AMOC) (Figure 7.2D) [Alonso-Garcia et al., 2011a]. Full glacial conditions were achieved in the third phase of glacial periods, where the AF was generally oriented east-to-west from Newfoundland to Ireland (Figure 7.2E) [Alonso-Garcia et al., 2011a]. During this phase large amounts of ice were accumulated on the continents, deep ocean circulation shifted to the glacial state in which deep-NADW was completely shut off, with more intermediate-depth glacial-NADW formation established [Alonso-Garcia et al., 2011a]. These conditions persisted until glacial terminations when the AF rapidly moved northwestwards

reaching a position similar to today, allowing the North Atlantic surface water mass to revert to the early interglacial phase within a few thousand years (Figure 7.2F) [Alonso-Garcia et al., 2011a]. The re-occurrence of these AF shifts in the NGS from MIS 19 to MIS 11 is consistent with the findings discussed here that strong lower NADW production persisted throughout all of the interglacial periods between MIS 19 and MIS 9. However, the location of the AF during the MPT was likely much different, with reduced inflow of surface waters from the NAC to the eastern-NGS, resulting in the decreased NADW production found prior to MIS 19.

Various studies from North Atlantic sites have suggested changes in the location of the interglacial AF throughout the MPT [Wright & Flower, 2002; Hernandez-Almeida et al., 2011; Marino et al., 2011]. Wright & Flower [2002] first proposed a northward shift of the interglacial AF during the MPT, likely reaching near-modern orientation around 600ka. Hernandez-Almeida et al. [2011] interpreted faunal shifts in radiolarian assemblages during interglacial periods after MIS 21 as a progressive northwest retreat of the AF, supported by diatom [Shimada et al., 2008] and alkenone [McClymont et al., 2008] assemblage data. They agreed with Wright & Flower [2002] that the interglacial AF position reached the same relative position it occupies today after ~610ka [Hernandez-Almeida et al., 2011]. Beginning in MIS 21, high levels of carbonate preservation, no nannofossil reworking, and no IRD input was found by Marino et al. [2011] in the north-east North Atlantic. These findings coincided with a shift in calcareous nannofossil fauna compared to the MIS 22 to MIS 35 time period beforehand, likely reflecting higher surface water temperature and the absence of sea-ice cover [Marino et al., 2011]. Following MIS 21, the records of Marino et al. [2011] are consistent with more pronounced glacial-interglacial AF variability, sea-ice extension, as well as more pronounced variability of deep and intermediate water mass production.

These studies, which support a progressive northwestward movement of the AF after MIS 21 from sites in the North Atlantic, are consistent with studies from within the NGS itself. Henrich et al. [2002] found that at the onset of the MPT (~1.2Ma), increased carbonate preservation from records of the southern NGS, Labrador Sea, and the northernmost North Atlantic occurred, suggesting an abrupt and nearly synchronous onset of the MPT. However, shifts within the western and northern regions of the NGS did not appear until ~0.9 to 0.7 Ma, when the character of the records change more gradually and the carbonate-bearing zone in the NGS progressively extends north-westward [Henrich & Baumann, 1994; Henrich et al., 2002]. During this time, increasing carbonate preservation and input of terrigenous sediments likely reflected the strengthening of the Norwegian Current during interglacial periods, and intensified glaciations on surrounding land-masses, respectively [Henrich & Baumann, 1994]. Helmke et al. [2003] found that glacial terminations equivalent to those of the late Pleistocene first occurred during the MIS 18/17 and MIS 20/19 transitions, indicated by minima in planktic $\delta^{18}O$ associated with the maxima in IRD accumulation. Following these events, the first full-interglacial conditions in the NGS develop during MIS 17 and MIS 19, respectively [Helmke et al., 2003]. The findings of Helmke et al. [2003] agree with the evidence presented here that strong NADW-influence throughout the deep Atlantic Ocean began at that time.

Following the progressive northwestward movement of the AF [Wright & Flower, 2002; Hernandez-Almeida et al., 2011; Marino et al., 2011], the onset of full interglacial conditions during MIS 19 and MIS 17 in the NGS [Henrich & Baumann, 1994; Henrich et al., 2002; Helmke et al., 2003] suggests a near modern influx of saline Atlantic-sourced surface waters [Alonso-Garcia et al., 2011a]. This influx of saline surface waters from the North Atlantic would increase NADW production within the region [Rahmstorf, 2002], consistent with the findings of

this study. Prior to this shift in interglacial AF location, NADW production in the NGS was likely completely (or nearly completely) due to brine rejection from winter sea-ice formation, similar to the region west of the AF today [Swift, 1986]. After MIS 19, the addition of more saline surface waters from the North Atlantic entering the NGS promoted enhanced production of NADW [Schmitz & McCartney, 1993; Rahmstorf, 2002].

7.4 Intensification of Glacial Terminations

The results discussed above provide evidence that NADW influence in the deep North Atlantic after MIS 17 initiated during glacial terminations. This production of the lower component of NADW during glacial terminations has also been found at other sites in the North Atlantic [Jones & Keigwin, 1988; Broecker and Denton, 1989; Lehman et al., 1991; Venz et al. 1999; Wright & Flower, 2002; Alonso-Garcia et al. 2011b]. During terminations, the AF shifted rapidly from its glacial position in the North Atlantic to its interglacial position within the NADW source region (NGS) within a few thousand years [Alonso-Garcia et al., 2011a]. I propose changing ice sheet dynamics led to the interglacial-AF shift to the northwest NGS after MIS 21, causing intensifying glacial terminations during this time period [Bintanja & van de Wal, 2008]. Glacial terminations are largely attributed to a series of positive feedbacks resulting in the collapse of continental ice sheets in the Northern Hemisphere [Clark et al., 1999; Maslin et al., 2001; Maslin & Ridgewell, 2005; Denton et al., 2010]. This implies a link between changing continental ice sheet dynamics and deep-water formation in the NGS during the MPT [Henrich et al., 2002; Clark et al., 2006; Hernandez-Almeida et al., 2012].

The onset of the MPT was accompanied by the first expanse of the Kara Sea Ice Sheet to the shelf break in the Arctic Ocean [Solheim et al., 1998; Knies et al., 2009]. After ~1Ma, the

Kara Sea Ice Sheet combined with the growing Barents Sea Ice Sheet in the northeastern-NGS [Knies et al., 2009], forming the northern-most component of the Eurasian Ice Sheet. The first grounding of the Kara Sea Ice Sheet on the submerged Yermak Plateau in the Arctic Ocean occurred at ~950ka [Solheim et al., 1998; Knies et al., 2007; Knies et al., 2009]. This time period is associated with significant increase in ice volume between MIS 24 and MIS 22 (Figure 2.1) [Head & Gibbard, 2005], corresponding to a drop in sea level of 20-30m [Kitamura & Kawagoe, 2006]. A continued drop in sea level likely contributed to the Barents Sea component of the Eurasian Ice Sheet first reaching the shelf edge in the NGS during glacial periods beginning with MIS 20 at ~800ka [Andreassen et al., 2004; Knies et al., 2009; Laberg et al., 2010; 2012]. Knies et al. [2007] provided conclusive evidence for five to six major terminations that likely succeeded shelf edge glaciations in the Barents Seas (supporting five to eight suggested by earlier studies [Mangerud et al., 1996; Sejrup et al., 2005]). During these terminations, prominent meltwater pulses occurred after the collapse of the Barents and Kara Sea ice sheets followed by eventual flooding of the eastern Kara Sea [Vogt et al., 2001; Vogt & Knies, 2008; Knies et al., 2009].

I propose that the expansion of ice sheets to the shelf edge in the northeastern-NGS was critical in intensifying glacial terminations, allowing the interglacial AF to migrate further north after MIS 21 [Hernandez-Almeida et al., 2011], and leading to the onset of full-interglacial conditions in the NGS first during MIS 19 and MIS 17 [Helmke et al., 2003]. Bintanja & van de Wal [2008] suggests a leading role for North American ice sheets initiating glacial terminations beginning during the MPT. Once these North American ice sheets reached a certain threshold size (of about 70 meter sea level equivalent), the following insolation maximum and associated air temperature peak triggered a rapid thinning of the ice sheet through increased basal sliding

rates [Clark et al., 1999; Marshall & Clark, 2002; Bintanja & van de Wal, 2008]. This would result in an initial rise in sea level, potentially undercutting and causing catastrophic failure of the Kara and Barents Sea Ice Sheet margins at the shelf edge [Clark et al., 1999; Maslin et al., 2001; Marshall & Clark, 2002; Maslin & Ridgewell, 2005]. This failure of ice sheet margins at the shelf edge would lead to an additional rise in sea level, flooding of the eastern Barents and Kara Sea [Vogt et al., 2001; Vogt & Knies, 2008; Knies et al., 2009]. The rapid nature of the collapse of ice sheet margins at the shelf edge in the NGS would allow for the introduction of enhanced inflow of surface waters from the NAC, driving NADW production in the NGS [Rahmstorf, 2002]. Overall, the timing of ice sheet advances to the shelf edge in the NGS during glacial periods after MIS 20, likely correspond with the rapid onset of NADW influence during glacial terminations in the intermediate (2000 to 3000m – after MIS 19) and deep (>4000m – after MIS 17) Atlantic Ocean. This provides evidence that large scale circulation changes during the MPT were likely caused by changing ice sheet dynamics, suggesting a leading role of Northern Hemisphere ice sheets for the global reorganization of the climate system throughout that time period in Earth's history.

	Avg δ13C values (per mil)									
Core Site	**MIS 9**	**MIS 11**	**MIS 13**	**MIS 15**	**MIS 17**	**MIS 19**	**MIS 21**	**MIS 25**	**MIS 27**	**MIS 29**
ODP 552	1.100	1.282	1.618	1.150	1.297	0.990	0.764	0.947	1.092	1.093
ODP 607	0.625	1.041	0.935	1.000	0.935	0.700	0.594	0.523	0.678	0.887
ODP 980	0.700	0.940	1.100	0.845	0.750	0.750	0.460	0.630	0.560	0.780
ODP 982	1.066	1.077	1.332	0.928	1.046	0.781	0.775	0.717	0.808	1.017
ODP 983	0.662	0.968	1.292	0.884	0.765	0.603	0.464	0.603	0.667	0.858
U-1308	0.585	0.838	1.039	0.801	0.641	0.655	0.414	0.594	0.455	0.601
ODP 1063	0.310	0.350	**0.800**	**0.330**	**0.414**	-0.170	-0.200	-0.080	-0.030	0.130
ODP 664	0.508	0.764	1.007	0.673	0.751	0.395	0.370	0.675	0.470	0.715
ODP 925	0.880	1.070	1.350	1.141	1.030	0.960				
ODP 927	0.670	1.180	1.090	0.978	0.740	0.780	0.500	0.580	0.820	
ODP 929		0.400	0.740	0.553	0.560	0.610	0.230	0.430	0.420	0.530
GeoB 1101	0.406	0.507	0.662							
RC13-229	-0.126	0.421	-0.336	-0.268	-0.668	-0.577				
GeoB 1034	0.550	0.747	0.838	0.258	0.483	0.128	0.189	0.333		
ODP 1088	0.215	0.582	0.762	0.482	0.536	0.270	0.287	0.319		
ODP 1089	-0.462	0.150	0.057	-0.131						
ODP 1090		0.060	0.377	-0.230	-0.052	-0.049	-0.120	-0.699	-0.616	-0.509

Table 7.1: The average $\delta^{13}C$ values from 17 sites, including Site 1063, during every interglacial period from MIS 9 to MIS 29, when applicable. These average $\delta^{13}C$ values were calculated from each site during interglacial maxima ($\delta^{18}O$ minima). This data was imported into Ocean Data View [Schlitzer, 2012] and used to construct the cross sections in Figure 7.1.

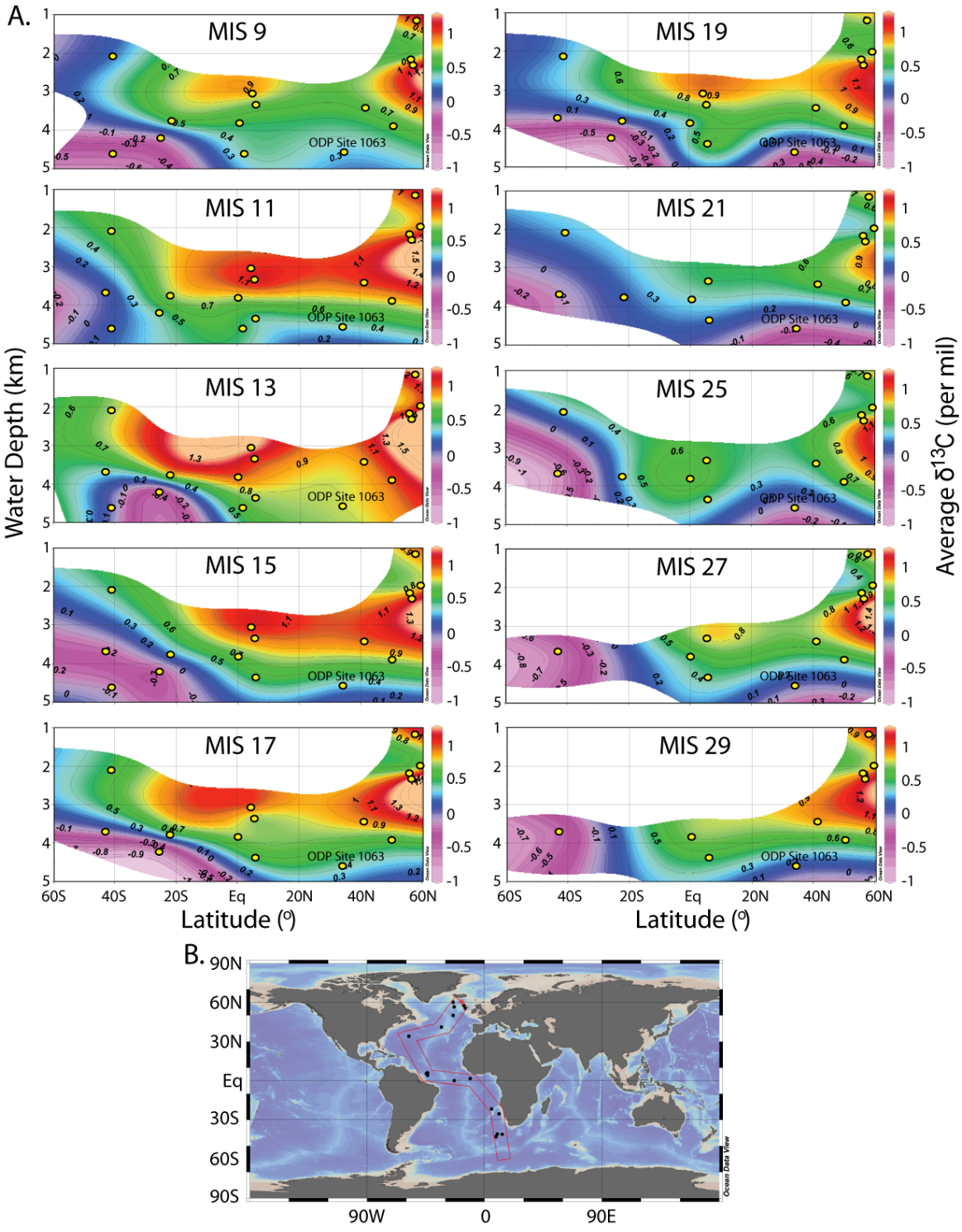

Figure 7.1: **A.** Cross section estimated distribution of $\delta^{13}C$ throughout the Atlantic Ocean for interglacial periods MIS 9, MIS 11, MIS 13, MIS 15, MIS 17, MIS 19, MIS 21, MIS 25, MIS 27, and MIS 29. These cross sections were constructed within Ocean Data View [Schlitzer, 2012] from the average $\delta^{13}C$ values in Table 7.1 along **B.** a transect connecting each site from 60°N to 60°S.

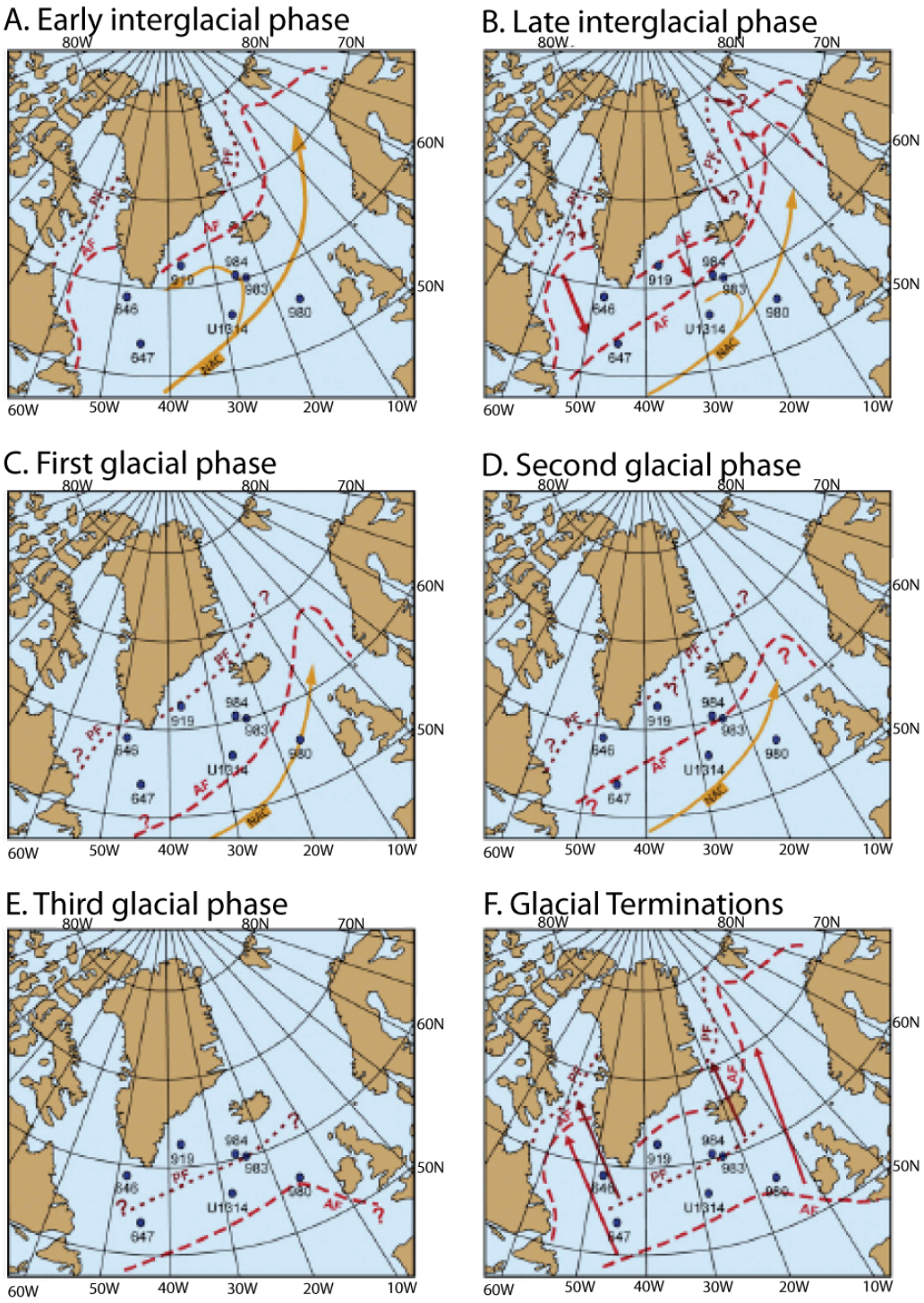

Figure 7.2: The location of the Arctic Front in relation to the five phases of glacial cycles (**A.** early interglacial phase; **B.** late interglacial phase; **C.** first glacial phase; **D.** second glacial phase; **E.** third glacial phase) and **F.** glacial terminations. This figure was originally from Alonso-Garcia et al. [2011a].

Chapter 8

CONCLUSIONS

This study provides evidence suggesting that a change in deep water circulation occurred at ODP Site 1063 beginning with the onset of MIS 17 (~700ka), supporting my hypothesis that circulation changes in the deep Atlantic Ocean were closely linked to the MPT. This evidence was found by filling a gap in the Site 1063 stable isotope record from ~500 to 750ka (MIS 13 to MIS 18), completing a continuous record from ~250 to 1030ka (MIS 8 to MIS 29). Within my study interval, I found relatively higher $\delta^{13}C$ during the interglacial periods MIS 13, MIS 15, and MIS 17 than during interglacials in the older section of the record [Ferretti et al., 2005]. These higher $\delta^{13}C$ persisted during the younger section of the record [Poli et al., 2000; Billups et al., 2011]. By comparing the Site 1063 $\delta^{13}C$ record with those from other sites in the North and South Atlantic source regions of NADW and AABW, respectively, I determined that an increase in NADW influence at Site 1063 was responsible for the higher interglacial $\delta^{13}C$ values after MIS 17. The glacial $\delta^{13}C$ values at Site 1063 remained low throughout the entire record, indicating the dominance of AABW influence at Site 1063 during glacial periods. Cross spectral analyses conducted between the $\delta^{18}O$ and $\delta^{13}C$ records reveal that they were nearly in phase at the eccentricity period, in phase at the obliquity period, and that $\delta^{18}O$ led $\delta^{13}C$ at the precession period. Addition cross spectral analyses were conducted on the time periods before and after the noted change in interglacial $\delta^{13}C$ values during MIS 17, revealing no change in the phase response at orbital periods.

To determine whether or not the intensification of NADW influence at Site 1063 during interglacial periods was also evident throughout the entire Atlantic Ocean, I constructed snap-shot

average interglacial $\delta^{13}C$ cross sections for each interglacial period between MIS 9 and MIS 29 from $60^{o}N$ to $60^{o}S$. By doing so, I found that NADW influence increased throughout the entire Atlantic Ocean beginning in MIS 19, propagating into the deepest region of the North Atlantic after MIS 17. This inferred enhanced production of the densest component of NADW likely occurred within the NGS during this time in relation to the progressive northwest movement of the AF. Based on the rapid onset of NADW production during glacial terminations, and the timing of glaciations reaching the shelf edge in the Arctic Ocean and Barents Seas in the northeastern NGS, this progressive AF movement likely coincided with glacial terminations becoming more intense. This could be explained by the buildup of thick ice sheets on glacial continental margins near sea-level in the Barents Sea. During glacial terminations, a small change in sea level would have undercut these marine-based ice margins, likely causing their catastrophic collapse. The first shelf edge glaciation of the Barents Sea ice sheet occurred during MIS 22. The AF began migrating to the northwest in the NGS during the succeeding MIS 21 interglacial period. Full interglacial conditions similar to those of the late Pleistocene developed during MIS 19 and MIS 17 in the NGS, immediately following glacial termination and corresponding to the major increase in NADW production found here within those interglacial periods. Ultimately, this study provides evidence for a close link between the MPT, ice sheet dynamics, and global ocean circulation.

REFERENCES

Aagaard, K., Fahrback, E., Meincke, J., Swift, J.H., 1991. Saline outflow from the Arctic Ocean: its contribution to deep waters of the Greenland, Norwegian, and Iceland Seas. Journal of Geophysical Research, 96, 20, 433-441.

Alonso-Garcia, M., Sierro, F.J., Flores, J.A., 2011a. Arctic front shifts in the subpolar North Atlantic during the Mid-Pleistocene (800-400 ka) and their implications for ocean circulation. Palaeogeography, Palaeoclimatology, Palaeoecology, 311, 268-280.

Alonso-Garcia, M., Sierro, F.J., Kucera, M., Flores, J.A., Cacho, I., Andersen, N., 2011b. Ocean circulation, ice sheet growth and interhemispheric coupling of millennial climate variability during the mid-Pleistocene (ca 800-400 ka). Quaternary Science Reviews, 30, 3234-3247.

Andreassen, K., Nilssen, L.C., Rafaelsen, B., Kuilman, L., 2004. Three-dimensional seismic data from the Barents Sea margin reveal evidence of past ice streams and their dynamics. Geology, 32, 729-732.

Bequey, S., Gersonde, R., 2002. Past hydrographic and climatic changes in the Subantarctic Zone of the South Atlantic – The Pleistocene record from ODP Site 1090. Palaeogeography, Palaeoclimatology, Palaeoecology, 182, 221-239.

Berger, A., Loutre, M.F., Insolation values for the climate of the last 10 million years. Quaternary Science Reviews, 10, 297-317.

Bickert, T., Curry, W.B., Wefer, G., 1997. Late Pliocene to Holocene (2.6-0 Ma) Western Equatorial Atlantic Deep-Water Circulation: Inferences from Benthic Stable Isotopes. Proceedings of the Ocean Drilling Program, Scientific Results, 154, 239-254.

Billups, K., Rabideaux, N., Stoffel, J., 2011. Suborbital-scale surface and deep water records in the subtropical North Atlantic: implications on thermohaline overturn. Quaternary Science Reviews, 30, 2976-2987.

Bintanja, R., van de Wal, R.S.W., 2008. North America ice-sheet dynamics and the onset of 100,000-year glacial cycles. Nature, 454, 869-872.

Bonisch, G., Schlosser, P., 1995. Deep water formation and exchange rates in the Greenland/Norwegian Seas and the Eurasian Basin of the Arctic Ocean derived from tracer balances. Progress in Oceanography, 35, 1, 29-52.

Born, A., Nisancioglu, K., Braconnot, P., 2010. Sea ice induced changes in ocean circulation during the Eemiam. Climate Dynamics, 35, 1361-1371.

Bower, A.S., Hunt, H.D., 2000. Lagrangian observations of the deep western boundary current in the North Atlantic Ocean. Part I: large-scale pathways and spreading rates. Journal of Physical Oceanography, 30, 764-783.

Broecker, W.S., Denton, G.H., 1989. The role of ocean-atmosphere reorganizations in glacial cycles. Geochimica et Cosmochimica Acta, 53, 10, 2465-2501.

Broecker, W.S., Donk, J., 1970. Insolation changes, ice volumes, and O18 record in deep-sea cores. Reviews of Geophysics, 8, 1, 169-198.

Channell, J.E.T., Hodell, D.A., Curtis, J.H., 2012. ODP Site 1063 (Bermuda Rise) revisited: Oxygen isotopes, excursions and paleointensity in the Brunhes Chron. Geochemistry, Geophysics, Geosytems, 13, 1, Q02001, doi:10.1029/2011GC003897.

Charles, C.D., Fairbanks, R.G., 1992. Evidence from Southern Ocean Sediments for the Effect of North Atlantic Deepwater Flux on Climate. Nature, 355, 416-419.

Clark, P.U., Alley, R.B., Pollard, D., 1999. Northern Hemisphere ice-sheet influences on global climate change. Science, 286, 1104-1111.

Clark, P.U., Archer, D., Pollard, D., Blum, J.D., Rial, J.A., Brovkin, V., Mix, A.C., Pisias, N.G., Roy, M., 2006. The middle Pleistocene transition: characteristics, mechanisms, and implications for long-term changes in atmospheric pCO_2. Quaternary Science Reviews, 25, 3150-3184.

Clark, P.U., Pollard, D., 1998. Origin of the middle Pleistocene transition by ice sheet erosion of regolith. Paleoceanography, 13, 1, 1-9.

Curry, W.B., Duplessy, J.C., Labeyrie, L.D., Shackleton, N.J., 1988. Changes in the distribution of d13C of deep water CO2 between the last glaciation and the Holocene. Paleoceanography, 3, 3, 317-341.

Denton, G.H., 2000. Does asymmetric thermohaline-ice-sheet oscillator drive 100,000-yr cycles. Journal of Quaternary Science, 15, 301-318.

Denton, G.H., Anderson, R.F., Toggweiler, J.R., Edwards, R.L., Schaefer, J.M., Putnam, A.E., 2010. The Last Glacial Termination. Science, 328, 1652-1656.

Dickson, R.R., Brown, J., 1994. The production of North Atlantic Deep Water: sources, rates, and pathways. Journal of Geophysical Research: Oceans, 99, C6, 12319-12341.

Dickson, A.J., Leng, M.J., Maslin, M.A., 2008. Mid-depth South Atlantic Ocean circulation and chemical stratification during MIS-10 to 12: Implications for atmospheric CO_2. Climate of the Past, 4, 333-344.

Emiliani, C., 1955. Pleistocene temperatures. The Journal of Geology, 538-578.

Fairbanks, R.G., 1989. A 17,000 year glacio-eustatic sea level record: influence of glacial melting rates on the Younger Dryas event and deep-ocean circulation, Nature, 342, 637-642.

Ferretti, P., Crowhurst, S.J., Hall, M.A., Cacho, I., 2010. North Atlantic millennial-scale climate variability 910 to 790 ka and the role of the equatorial insolation forcing. Earth and Planetary Science Letters, 293, 28-41.

Ferretti, P., Shackleton, N.J., Rio, D., Hall, M.A., 2005. Early-Middle Pleistocene deep circulation in the western subtropical Atlantic: Southern Hemisphere modulation of the North Atlantic Ocean. In: Head, M.J., Gibbard, P.L., (Eds.), Early-Middle Pleistocene Transitions: The Land Ocean Evidence 247. The Geological Society, London, 131-145.

Flower, B.P., Oppo, D.W., McManus, J.F., Venz, K.A., Hodell, D.A., Cullen, J.L., 2000. North Atlanic intermediate to deep water circulation and chemical stratification during the past 1 Myr. Paleoceanography, 15, 4, 388-403.

Gildor, H., Tziperman, E., 2000. Sea ice as the glacial cycles' climate switch: Role of seasonal and orbital forcing. Paleoceanography, 15, 6, 605-615.

Grützner, J., Giosan, L., Franz, S.O., Tiedemann, R., Cortijo, E., Chaisson, W.P., Flood, R.D., Hagen, S., Keigwin, L.D., Poli, S., Rio, D., Williams, T., 2002. Astronomical age models for Pleistocene drift sediments from the western North Atlantic (ODP Sites 1055-1063). Marine Geology, 189, 5-23.

Haley, B.A., Frank, M., Spielhagen, R.F., Eisenhauer, A., 2008. Influence of brine formation on Arctic Ocean circulation over the past 15 million years. Nature, 1, 68-72.

Haley, B.A., Polyak, L., 2013. Pre-modern Arctic Ocean circulation from surface sediment neodymium isotopes. Geophysical Research Letters, 40, 1-5, doi:10.1002/GRL.50188.

Hays, J.D., Imbrie, J., Shackleton, N.J., 1976. Variations in the Earth's orbit: Pacemaker of the ice ages. Science, 194, 4270, 1121-1132.

Head, M.J., Gibbard, P.L., eds. 2005. *Early-Middle Pleistocene Transitions: The Land-Ocean Evidence.* London: Geological Society of London.

Head, M.J., Pillans, B., Farquhar, S.A., 2008. The Early-Middle Pleistocene Transition: characterization and proposed guide for the defining boundary. Episodes 31.2, 255.

Helmke, J.P., Bauch, H.A., Erlenkeuser, H., 2003. Development of glacial and interglacial conditions in the Nordic seas between 1.5 and 0.35 Ma. Quaternary Science Reviews, 22, 1717-1728.

Henrich, R., Baumann, K.H., 1994. Evolution of the Norwegian Current and the Scandinavian Ice Sheets during the past 2.6 m.y.: evidence from ODP Leg 104 biogenic carbonate and terrigenous records. Palaeogeography, Palaeoclimatology, Palaeoecology, 108, 75-94.

Henrich, R., Baumann, K.H., Huber, R., Meggers, H., 2002. Carbonate preservation records of the past 3 Myr in the Norwegian-Greenland Sea and the northern North Atlantic: implications for the history of NADW production. Marine Geology, 184, 1, 17-39.

Hernandez-Almeida, I., Bjoklund, K.R., Sierro, F.J., Filippelli, G.M., Cacho, I., Flores, J.A., 2011. A high resolution opal and radiolarian record from the subpolar North Atlantic during the Mid-Pleistocene Transition (1069-779 ka): Paleoceanographic implications. Palaeogeography, Palaeoclimatology, Palaeoecology, doi:10.1016/j.palaeo.2011.05.049.

Hodell, D.A., Channell, J.E.T., Curtis, J.H., Romero, O.E., Rohl, U., 2008. Onset of "Hudson Strait" Heinrich events in the eastern North Atlantic at the end of the middle Pleistocene transition (~640 ka)? Paleoceanography, 23, PA4218, doi:10.1029/2008PA001591.

Hodell, D.A., Charles, C.D., Ninnemann, U.S., 2000. Comparison of interglacial stages in the South Atlantic sector of the southern ocean for the past 450 kyr: implications for Marine Isotope Stage (MIS) 11. Global and Planetary Change, 24, 7-26.

Hodell, D.A., Venz-Curtis, K.A., 2006. Late Neogene history of deepwater ventilation in the Southern Ocean. Geochemistry, Geophysics, Geosystems, 7, 9, doi:10.1029/2005GC001211.

Hoogakker, B.A.A., McCave, I.N., Vautravers, M.J., 2007. Antarctic link to deep flow speed variation during Marine Isotope Stage 3 in the western North Atlantic. Earth and Planetary Science Letters, 257, 463-473.

Imbrie, J., Berger, A., Boyle, E.A., Clemens, S.C., Duffy, A., Howard, W.R., Kukla, G., Kutzbach, J., Martinson, D.G., McIntyre, A., Mix, A.C., Molfino, B., Morley, J.J., Peterson, L.C., Pisias, N.G., Prell, W.L., Raymo, M.E., Shackleton, N.J., Toggweiler, J.R., 1993. On the structure and origin of major glaciation cycles 2: The 100,000-year cycle. Paleoceanography, 8, 6, 699-735.

Imbrie, J., Boyle, E.A., Clemens, S.C., Duffy, A., Howard, W.R., Kukla, G., Kutzbach, J., Martinson, D.G., McIntyre, A., Mix, A.C., Molfino, B., Morley, J.J., Peterson, L.C., Pisias, N.G., Prell, W.L., Raymo, M.E., Shackleton, N.J., Toggweiler, J.R., 1992. On the structure and origin of major glaciation cycles 1: Linear responses to Milankovich forcing. Paleoceanography, 7, 6, 701-738.

Johannessen, T., Jansen, E., Flatoy, A., Ravelo, A.C., 1994. The relationship between surface water masses, oceanographic fronts and paleoclimatic proxies in surface sediments of the Greenland, Iceland, Norwegian Seas. Nato ASI Series, 117, 61-85.

Jones, G.A., Keigwin, L.D., 1988. Evidence from Fram Strait (78 N) for early deglaciation. Nature, 336, 6194, 56-59.

Katz, M.E., Katz, D.R., Wright, J.D., Miller, K.G., Pak, D.K., Shackleton, N.J., Thomas, E., 2003. Early Cenozoic benthic foraminiferal isotopes: Species reliability and interspecies correction factors. Paleoceanography, 18, 2, 1024, doi:10.1029/2002PA000798.

Keigwin, L.G., Jones, G.A., 1994. Western North Atlantic evidence for millennial-scale changes in ocean circulation and climate. Journal of Geophysical Research, 99, 12,397-12,410.

Keigwin, L.D., Rio, D., Acton, G.D., et al., 1998. Proceedings of the Ocean Drilling Program. Initial Report, 172, 77-156.

Kennett, J., Cannariato, K.G., Hendy, I.L., Behl, R.J., 2003. Methane hydrates in Quaternary climate change: The clathrate gun hypothesis. American Geophysical Union, 216.

Kitamura, A., Kawagoe, T., 2006. Eustatic sea-level change at the Mid-Pleisotocene climate transition: new evidence from the shallow-marine sediment record of Japan. Quaternary Science Reviews, 25, 325-335.

Knies, J., Matthiessen, J., Mackensen, A., Stein, R., Vogt, C., Frederichs, T., Nam, S.-I., 2007. Effects of Arctic freshwater forcing on thermohaline circulation during the Pleistocene. Geology, 35, 1075-1078.

Knies, J., Matthiessen, J., Vogt, C., Laberg, J.S., Hjelstuen, B.O., Smelror, M., Larsen, E., Andreassen, K., Eidvin, T., Vorren, T.O., 2009. The Plio-Pleistocene glaciation of the Barents Sea-Svalbard region: a new model based on revised chronostratigraphy. Quaternary Science Reviews, 28, 812-829.

Kroopnick, P.M., 1980. The distribution of ^{13}C in the Atlantic Ocean: Earth and Planetary Science Letters, 49, 469-484.

Laberg, J.S., Andreassen, K., Knies, J., Vorren, T.O., Winsborrow, M., 2010. Late Plio-Pleistocene development of the Barents Sea ice sheet. Geology, 38, 107-110.

Laberg, J.S., Andreassen, K., Vorren, T.O., 2012. Late Cenozoic erosion of the high-latitude southwestern Barents Sea shelf revisited. GSA Bulletin, 124, 1-2, 77-88.

Lehman, S., Jones, G.A., Keigwin, L.D., Andersen, E.S., Butenkoi, G., Ostmo, S.R., 1991. Initiation of Fennoscandian ice-sheet retreat during the last deglaciation. Nature, 349, 513-516.

Lisiecki, L.E., Raymo, M.E., Curry, W.B., 2008. Atlantic overturning responses to Late Pleistocene climate forcings. Nature, 456, doi:10.1038/nature07425.

Lisiecki, L.E., & Raymo, M.E., 2005. A Pliocene-Pleistocene stack of 57 globally distributed benthic $\delta^{18}O$ records. Paleoceanography, 20, 1, 1-17.

Mackensen, A., Hubberten, H.W., Bickert, T., Fischer, G., Futterer, D.K., 1993. The $\delta^{13}C$ in benthic foraminiferal tests of Fontbotia wuellerstorfi (Schwager) Relative to the $\partial^{13}C$ of dissolved inorganic carbon in Southern Ocean Deep Water: Implications for glacial ocean circulation models. Paleoceanography, 8, 5, 587-610.

Mangerud, J., Jansen, E., Landvik, J.Y., 1996. Late Cenozoic history of the Scandinavian and Barents Sea ice sheets. Golbal and Planetary Change, 12, 11-26.

Marchal, O., Curry, W.B., 2008. On the Abyssal Circulation in the Glacial Atlantic. Journal of Physical Oceanography, 38, doi:10.1175/2008JPO3895.1.

Marino, M., Maiorano, P., Flower, B.P., 2011. Calcareous nannofossil changes during the Mid-Pleistocene Revolution: Paleoecologic and paleoceanographic evidence from North Atlantic Site 980/981. Palaeogeography, Palaeoclimatology, Palaeoecology, 306, 58-69.

Marshall, S.J., Clark, P.U., 2002. Basal temperature evolution of North American ice sheets and implications for the 100-kyr cycle. Geophysical Research Letters, 29, doi:10.1029/2002GL015192.

Maslin, M.A., Ridgewell, A.J., 2005. Mid-Pleistocene revolution and the 'eccentricity myth.' Geological Society, London. Special Publications 247.1, 19-34.

Maslin, M.A., Seidov, D., Lowe, J., 2001. Synthesis of the nature and causes of sudden climate transitions during the Quaternary. In: Seidov, D., Haup, B., Maslin, M.A., eds. The oceans and rapid climate change: past, present, and future. AGU Geophysical Monograph Series, 126, 9-52.

McCartney, M.S., Talley, L.D., 1982. The subpolar mode water of the North Atlantic Ocean. Journal of Physical Oceanography, 12, 11, 1169-1188.

McCartney, M.S., Talley, L.D., 1984. Warm-to-cold water conversion in the northern North Atlantic Ocean. Journal of Physical Oceanography, 14, 5, 922-935.

McCave, I.N., Manighetti, B., Robinson, S.G., 1995. Sortable Silt and fine sediment size/composition slicing: Parameters for palaeocurrent speed and paleoceanography. Paleoceanography, 10, 3, 593-610.

McCave, I.N., Tucholke, B.E., 1986. Deep current-controlled sedimentation in the western North Atlantic, M, Geological Society of America, Boulder, 451-468.

McClymont, E.L., Rosell-Mele, A., Haug, G.H., Lloyd, J.M., 2008. Expansion of subarctic water masses in the North Atlantic and Pacific oceans and implications for mid-Pleistocene ice sheet growth. Paleoceanography, 23, PA4214, doi:10.1029/2008PA001622.

Mix, A.C., Le, J., Shackleton, N.J., 1995a. Benthic foraminiferal stable isotope stratigraphy of site 846: 0-1.8 Ma.

Mix, A.C., Pisias, N.G., Rugh, W., Wilson, J., Morey, A., 1995b. Benthic foraminifer stable isotope record from Site 849 (0-5Ma): local and global climate changes. Proceedings of the Ocean Drilling Program, Scientific Results.

Muller, R.A., MacDonald, G.J., 1997. Glacial cycles and astronomical forcing. Science, 277, 215-218.

Oppo, D.W., Lehman, S.J., 1995. Suborbital timescale variability of North Atlantic Deep Water during the past 200,000 years. Paleoceanography, 10, 5, 901-910.

Ostermann, D.R., Curry, W.B., 2000. Calibration of stable isotopic data: an enriched $\delta^{18}O$ standard used for source gas mixing detection and correction. Paleoceanography, 15, 3, 353-360.

Paul, J.R., Berger, W.H., 1999. Climate cycles and climate transitions as a response to astronomical and CO_2 forcings. In Harff, J., Lemke, W., Stattegger, K. (eds.) Computerized modeling of sedimentary systems. Springer-Verlag, Berlin, Heidelberg, 223-245.

Poli, M.S., Thunell, R.C., Rio, D., 2000. Millenial-scale changes in North Atlantic Deep Water circulation during marine isotope stage 11 and 12: Linkage to Antarctic climate. Geology, 28, 9, 807-810.

Rahmstorf, S., 2002. Ocean circulation and climate during the past 120,000 years. Nature, 419, 207-214.

Raymo, M.E., 1997. The timing of major climate terminations. Paleoceanography, 12, 4, 577-585.

Raymo, M.E., Oppo, D.W., Curry, W., 1997. The mid-Pleistocene climate transition: A deep sea carbon isotopic perspective. Paleoceanography, 12, 4, 546-559.

Raymo, M.E., Oppo, D.W., Flower, B.P., Hodell, D.A., McManus J.F., Venz, K.A., Kleiven, K.F., McIntyre, K., 2004. Stability of North Atlantic water masses in face of pronounced climate variability during the Pleistocene. Paleoceanography, 19, PA2008, doi:10.1029/2003PA000921.

Raymo, M.E., Ruddiman, W.F., Shackleton, N.J., Oppo, D.W., 1990. Evolution of Atlantic-Pacific d13C gradients over the last 2.5 m.y. Earth and Planetary Science Letters, 97, 353-368.

Rubinson, M., Clayton, R.N., 1969. Carbon-13 fractionation between aragonite and calcite. Geochimica et Cosmochimica Acta 33, 8, 997-1002.

Ruddiman, W.F., Raymo, M.E., 2003. A methane-based time scale for Vostok ice. Quaternary Science Reviews, 22, 141-155.

Saltzman, B., 2001. Dynamical Paleoclimatology: generalized theory of global climate change. Academic Press, San Diego, p. 320.

Schlitzer, R., Ocean Data View, http://odv.awi.de, 2012.

Schmitz Jr., W.J., McCartney, M.S., 1993. On the North Atlantic Circulation. Reviews of Geophysics, 31, 1, 29-49.

Sejrup, H.P., Hjelstuen, B.O., Dahlgren, K.I.T., Haflidason, H., Kuijpers, A., Nygard, A., Praeg, D., Stoker, M.S., Vorren, T.O., 2005. Pleistocene glacial history of the NW European continental margin. Marine Petroleum Geology, 22, 1111-1129.

Shackleton, N.J., 1967. Oxygen isotope analyses and Pleistocene temperatures re-assessed. Nature, 215, 5096, 15-17.

Shackleton, N.J., 1977. Oxygen isotope and palaeomagnetic evidence for early Northern Hemisphere glaciation. Nature, 270, 216-219.

Shackleton, N.J., 2000. The 100,000-year ice-age cycle identified and found to lag temperature, carbon dioxide, and orbital eccentricity. Science, 289, 5486, 1897-1902.

Shackleton, N.J., Opdyke, N.D., 1976. Oxygen-isotope and paleomagnetic stratigraphy of Pacific core V28-239 late Pliocene to latest Pleistocene. Geological Society Am. Mem., 145, 449-464.

Shimada, C., Sato, T., Toyoshima, S., Yamasaki, M., Tanimura, Y., 2008. Paleoecological significance of laminated diatomaceous oozes during the middle-to-late Pleistocene, North Atlantic Ocean (IODP Site U1304), Marine Micropaleontology, 69, 2, 139-150.

Solheim, A., Faleide, J.I., Andersen, E.S., Elverhoi, A., Forsberg, C.F., Vanneste, K., Uenzelmann-Neben, G., Channell, J.E.T., 1998. Late Cenozoic Seismic Stratigraphy and Glacial Geological Development of the East Greenland and Svalbard-Barents Sea Continental Margins. Quaternary Science Reviews, 17, 1-3, 155-184.

Spero, H.J., Bijima, J., Lea, D.W., Bemis, B.E., 1997. Effect of seawater carbonate concentration on planktonic foraminiferal carbon and oxygen isotopes. Nature, 390, 497-500.

Spero, H.J., Lerche, I, Williams, D.F., 1991. Opening the carbon isotope "vital effect" black box, 2: Quantitative model for interpreting foraminiferal carbon isotope data. Paleoceanography, 6, 639-655.

Stahr, F.R., Sanford, T.B., 1999. Transport and bottom boundary layer observations of the North Atlantic Deep Western Boundary Current at the Blake Outer Ridge. Deep-Sea Research Part II – Tropical Studies in Oceanography, 46, 205-243.

Swift, J.H., 1986. The arctic wates. The Nordic Seas. Springer New York, 129-154.

Swift, J.H., Aagaard, K., 1981. Seasonal transitions and water mass formation in the Iceland and Greenland seas. Deep Sea Research Part A. Oceanographic Research Papers, 28, 10, 1107-1129.

Thornally, D.J.R., Barker, S., Becker, J., Knorr, G., Hall, I.R., 2013. Abrupt changes in deep Atlantic circulation during the transition to full glacial conditions. Paleoceanography, doi:10.1002/palo.20025.

Tziperman, E., Gildor, H., 2003. On the mid-Pleistocene transition to 100-kyr glacial cycles and the asymmetry between glaciation and deglaciation times. Paleoceanography, 18, 1, 1-8.

Venz, K.A., Hodell, D.A., Stanton, C., Warnke, D.A., 1999. A 1.0 Myr record of Glacial North Atlantic Intermediate Water variability from ODP site 982 in the northeast Atlantic. Paleoceanography, 14, 1, 42-52.

Vogt, C., Knies, J., Spielhagen, R.F., Stein, R., 2001. Detailed mineralogical evidence for two nearly identical glacial/deglacial cycles and Atlantic water advection to the Arctic Ocean during the last 90,000 years. Global and Planetary Change, 31, 23-44.

Vogt, C., Knies, J., 2008. Sediment dynamics in the Eurasian Arctic Ocean during the last deglaciation – the clay mineral group smectite perspective. Marine Geology, 250, 211-222.

Wright, A.K., Flower, B.P., 2002. Surface and deep ocean circulation in the subpolar North Atlantic during the mid-Pleistocene revolution. Paleoceanography, 17, 4, 1068, doi:10.1029/2002PA000782.

Zachos, J., Pagani, M., Sloan, L., Thomas, E., Billups, K., 2001. Trends, Rhythms, and Abbreviations in Global Climate 65 Ma to Present. Science, 292, 686-693.

APPENDIX A

ODP SITE 1063 STABLE ISOTOPE DATA FROM MIS 13 TO MIS 18

Meters Composite Depth (mcd)	Age - ka (Channell age model)	**Age - ka (tuned to LR04)**	**δ18O (per mil)**	**δ13C (per mil)**
108.36	517.50	499.31	3.13	0.83
108.46	517.92	500.44	3.23	1.01
108.51	518.13	501.00	3.09	1.01
108.56	518.35	501.59	3.07	0.88
108.61	518.57	502.18	3.08	0.77
108.66	518.78	503.06	3.47	1.22
108.71	519.00	503.99	3.38	-0.05
108.76	519.21	504.89	3.49	0.21
108.81	519.42	505.78	3.59	-0.26
108.86	519.63	506.67	2.97	1.14
108.96	520.04	507.35	3.21	0.20
109.01	520.26	507.61	3.42	0.57
109.06	520.48	507.87	3.40	0.03
109.11	520.70	508.13	3.64	0.82
109.16	520.91	508.37	3.61	0.95
109.21	521.13	508.63	3.64	0.77
109.26	521.33	508.91	3.43	0.94
109.31	521.54	509.54	3.80	1.20
109.36	521.75	510.17	3.70	1.14
109.41	521.96	510.80	3.66	0.98
109.46	522.17	511.72	3.63	0.09
109.51	522.39	512.91	3.76	1.20
109.61	522.83	515.28	3.84	1.22
109.66	523.04	516.26	3.33	1.25
109.71	523.25	516.70	4.03	1.22
109.76	523.46	517.13	3.71	1.13
109.81	523.67	517.55	3.97	1.15
109.86	523.88	517.97	3.64	0.99
109.91	524.09	518.39	3.63	1.26
109.96	524.30	518.82	3.64	1.16
110.01	524.52	519.26	3.88	1.21
110.06	524.74	519.70	3.55	1.03
110.11	524.96	520.15	3.67	1.15
110.16	525.17	520.57	3.91	0.98
110.21	525.38	520.99	3.75	1.24
110.31	525.79	521.78	3.28	0.59
110.41	526.22	522.35	4.14	0.87
110.56	526.87	523.21	3.35	0.66
110.61	527.08	523.48	4.07	0.82
110.66	527.29	523.76	3.28	-0.38
110.71	527.50	524.20	3.47	0.44
110.86	528.13	525.74	3.81	0.57
110.91	528.35	526.27	4.25	-0.02
111.06	529.00	527.80	3.43	-0.53
111.11	529.21	528.15	4.21	0.50
111.16	529.42	528.51	3.62	-0.53
111.21	529.63	528.86	3.76	-0.87
111.26	529.83	529.20	4.39	-0.14
111.31	530.04	529.55	4.06	-0.34
111.41	530.48	530.29	3.57	-0.47
111.46	530.70	530.66	3.84	-0.17
111.56	531.13	531.39	4.32	-0.55
111.61	531.33	531.73	3.92	-0.22
111.66	531.54	532.08	4.41	0.20

Meters Composite Depth (mcd)	Age - ka (Channell age model)	**Age - ka (tuned to LR04)**	**δ18O (per mil)**	**δ13C (per mil)**
111.69	531.67	532.30	4.02	0.08
111.71	531.75	532.43	4.40	0.32
111.74	531.88	532.65	3.86	-0.28
112.29	534.22	536.62	4.61	-0.26
112.64	535.71	539.51	4.45	-0.26
112.79	536.35	540.96	3.94	-0.57
112.84	536.57	541.46	3.24	0.67
112.99	537.21	542.91	4.08	0.31
113.04	537.42	543.39	3.94	-0.15
113.09	537.63	543.74	3.67	-0.17
113.19	538.05	544.12	4.02	0.16
113.24	538.29	544.34	4.28	0.27
113.29	538.52	544.55	3.97	0.06
113.84	541.67	547.90	4.45	-0.32
113.89	542.00	548.59	3.97	-0.43
113.99	542.67	551.16	3.92	-0.07
114.09	543.33	551.48	3.91	-0.10
114.14	543.67	551.62	4.18	0.14
114.29	544.67	552.03	3.88	0.14
114.34	545.00	552.17	4.40	0.38
114.39	545.36	552.32	3.82	-0.03
114.49	546.07	552.61	3.78	-0.16
114.54	546.43	552.76	3.95	0.20
114.59	546.79	552.91	3.75	-0.45
114.64	547.14	553.05	3.78	-0.05
114.69	547.50	553.20	3.82	-0.08
114.74	547.86	553.35	3.74	0.07
114.79	548.21	553.49	3.85	-0.59
114.89	548.93	553.79	3.83	0.02
114.94	549.27	553.93	3.54	0.09
115.04	549.93	555.02	3.74	-0.02
115.09	550.29	555.89	3.80	-0.22
115.14	550.64	556.73	4.06	-0.60
115.19	551.00	557.60	3.51	0.15
115.29	551.71	559.32	3.29	0.28
115.39	552.43	560.20	3.37	-0.31
115.44	552.79	560.60	4.32	0.19
115.49	553.14	560.99	3.57	-0.26
115.54	553.50	561.39	4.15	0.32
115.59	553.86	561.79	3.80	0.48
115.64	554.21	562.17	3.33	0.30
116.09	557.43	565.38	3.87	0.57
116.14	557.79	565.73	3.43	0.61
116.19	558.15	566.08	3.08	0.72
116.24	558.54	568.83	3.33	0.76
116.29	558.92	571.73	2.89	-0.11
116.34	559.31	573.45	3.15	0.50
116.39	559.69	574.01	3.30	
116.49	560.46	575.16	3.06	0.60
116.54	560.85	575.80	2.28	0.23
116.59	561.27	576.44	2.86	0.41
116.64	561.73	577.00	2.98	
116.69	562.18	577.56	2.95	0.30
116.74	562.64	578.12	2.87	0.82

Appendix A (continued)

Meters Composite Depth (mcd)	Age - ka (Channell age model)	**Age - ka (tuned to LR04)**	**δ18O (per mil)**	**δ13C (per mil)**
116.79	563.09	578.63	2.80	0.28
116.84	563.55	578.95	3.14	0.49
116.89	564.00	579.26	3.47	0.63
116.94	564.42	579.55	3.00	0.64
116.99	564.83	579.84	3.28	0.82
117.04	565.30	580.16	2.86	0.50
117.09	565.80	580.51	3.30	0.92
117.44	570.14	583.52	3.86	-0.16
117.49	570.86	584.01	3.69	0.17
117.54	571.50	584.46	3.86	0.02
117.59	572.14	584.78	3.98	0.19
117.74	574.14	585.73	3.84	0.07
117.79	574.86	586.07		0.11
117.84	575.50	586.37		0.23
117.94	576.86	587.01	3.75	-0.37
118.09	578.86	587.88	3.61	0.15
118.19	580.14	588.41	3.98	0.07
118.24	580.86	588.70	4.03	0.72
118.29	581.50	588.97	3.68	0.91
118.34	582.14	589.21	3.29	0.27
118.39	582.86	589.51	4.04	1.25
118.44	583.50	589.77	3.53	0.87
118.63	586.00	591.12	3.94	0.87
118.64	586.14	591.20	3.78	-0.38
118.93	590.00	593.35	3.85	0.27
118.98	590.71	593.75	3.72	-0.11
119.03	591.38	594.13	3.42	-0.04
119.08	592.00	594.66	3.54	0.53
119.13	592.71	595.36	3.37	0.67
119.18	593.38	596.02	3.26	0.59
119.23	594.00	596.61	2.91	0.55
119.28	594.63	597.13	3.65	0.83
119.33	595.29	597.68	3.19	0.35
119.38	596.00	598.28	3.47	0.42
119.43	596.63	598.80	3.11	0.12
119.48	597.29	599.35		0.85
119.53	598.00	599.95	3.29	0.41
119.58	598.63	600.47	3.50	0.41
119.63	599.29	601.02	3.24	0.32
119.68	600.00	601.62	3.31	0.13
119.73	600.63	602.16		
119.78	601.29	602.70	3.48	-0.22
119.98	604.00	604.96	2.93	0.13
120.13	605.88	608.15	2.97	
120.18	606.44	609.42	2.86	0.22
120.23	607.00	610.69	3.46	0.78
120.43	608.91	615.03	2.37	0.55
120.48	609.33	616.06	2.02	
120.53	609.75	616.86	3.16	0.51
120.58	610.18	617.64	3.19	0.32
120.63	610.64	618.48	3.55	0.44
120.68	611.09	619.30	3.43	0.69
120.73	611.55	620.14	3.44	0.38
120.83	612.42	621.04	3.37	0.33

Meters Composite Depth (mcd)	Age - ka (Channell age model)	**Age - ka (tuned to LR04)**	**δ18O (per mil)**	**δ13C (per mil)**
120.88	612.83	621.32	3.75	-0.45
121.18	615.55	623.57	4.04	-0.68
121.23	616.00	624.64	4.25	-0.69
121.28	616.38	625.54	4.56	-0.28
121.33	616.77	626.97	4.59	-0.20
121.88	621.15	628.54	4.52	-0.64
122.74	627.13	629.64	4.59	-0.74
123.54	631.58	630.46	4.64	-0.78
125.34	638.67	631.76	4.58	-0.26
125.64	639.65	633.30	4.50	-0.41
125.69	639.81	633.61	4.09	-0.89
125.84	640.29	634.17	4.71	-0.47
125.94	640.61	634.53	3.98	-0.69
126.04	640.94	634.88	4.44	-0.11
126.34	641.76	635.74	4.86	-0.76
126.81	642.81	636.85	4.39	-0.24
127.06	643.34	637.22	4.44	-0.19
127.61	644.51	638.10	4.37	-0.65
127.71	644.72	638.37	4.30	-0.59
127.91	645.15	639.34	4.45	-0.39
128.21	645.79	641.15	4.53	-1.02
128.31	646.00	641.79	3.79	-0.54
128.41	646.21	642.33	4.34	-0.36
128.51	646.43	642.88	4.22	-0.17
128.66	646.74	643.65	4.13	-0.53
128.71	646.85	643.92	4.15	-0.84
128.81	647.06	644.44	4.15	-0.93
128.86	647.17	644.72	4.17	-0.71
128.96	647.38	645.24	4.20	-0.53
129.01	647.49	645.51	4.25	-0.65
129.06	647.60	645.79	4.30	-0.06
129.21	647.91	646.56	4.02	-0.71
129.76	649.14	649.62	4.16	-0.49
129.81	649.27	649.94	3.94	-0.56
129.86	649.41	650.50	4.04	-0.32
129.91	649.54	651.09	4.15	-0.48
129.96	649.68	651.72	4.23	-0.40
130.01	649.81	652.31	4.35	-0.34
130.06	649.95	652.95	4.15	0.01
130.11	650.08	653.54	4.49	0.21
130.16	650.22	654.17	4.17	-1.09
130.21	650.36	654.80	4.18	-0.59
130.31	650.64	656.07	3.92	0.06
130.46	651.06	657.05	4.11	-0.25
130.56	651.39	657.82	4.39	-0.14
130.76	652.03	659.30	3.79	-0.23
130.81	652.19	659.85	4.00	0.26
130.86	652.35	660.48	4.11	-0.58
130.91	652.52	661.14	4.21	-0.39
131.06	653.00	663.03	4.06	-0.43
131.11	653.17	663.65	3.97	-0.23
131.16	653.34	663.93	4.14	-0.31
131.21	653.52	664.22	4.05	-0.10
131.26	653.69	664.50	4.16	-0.14

Appendix A (continued)

Meters Composite Depth (mcd)	Age - ka (Channell age model)	**Age - ka (tuned to LR04)**	**δ18O (per mil)**	**δ13C (per mil)**
131.31	653.86	664.77	3.90	-0.39
131.36	654.04	665.07	4.01	-0.54
131.41	654.21	665.34	4.00	-0.04
131.46	654.39	665.64	3.70	0.00
131.56	654.75	666.47	4.00	0.01
131.61	654.93	666.88	3.75	-0.45
131.66	655.12	667.17	4.02	-0.66
131.71	655.32	667.47	4.20	-0.22
131.76	655.52	667.77	4.10	-1.05
131.86	655.92	668.37	4.01	-0.78
131.91	656.12	668.67	3.91	-0.21
131.96	656.32	668.97	3.98	-0.40
132.01	656.52	669.28	3.58	-0.59
132.06	656.72	669.62	3.85	0.13
132.11	656.92	670.00	4.09	-1.21
132.51	658.57	672.79	3.87	-0.88
132.56	658.78	672.99	3.93	-0.91
132.61	659.00	673.19	3.63	-0.64
132.71	659.42	673.58	3.98	-0.12
132.76	659.63	673.77	3.98	-0.74
132.96	660.48	674.56	3.78	-1.20
133.01	660.70	674.76	3.83	-0.46
133.06	660.91	674.96	3.58	-0.56
133.11	661.17	675.20	3.80	-0.19
133.16	661.44	675.45	3.73	0.03
133.21	661.72	675.70	3.93	-0.82
133.26	662.00	675.96	3.91	0.15
133.46	663.33	677.19	3.60	-1.07
134.06	667.36	678.95	3.25	-1.35
134.11	667.71	679.25	4.03	-1.12
134.21	668.43	679.87	3.38	-0.89
134.26	668.79	680.18	3.53	-0.65
134.31	669.15	680.49	3.74	-0.29
134.36	669.54	680.83	3.55	-0.62
134.41	669.92	681.16	3.32	-0.65
134.46	670.31	681.49	3.42	-0.15
134.51	670.69	681.82	3.14	-0.06
134.56	671.08	682.15	3.50	-0.72
134.61	671.50	682.52	3.56	-0.65
134.66	671.92	682.88	3.61	-0.64
134.71	672.31	683.21	3.92	-0.17
134.76	672.69	683.54	3.83	-0.59
134.81	673.08	683.88	3.43	-0.40
134.86	673.46	684.20	3.34	-0.83
134.91	673.85	684.43	3.12	-0.31
134.96	674.25	684.55	3.57	-0.64
135.04	674.92	684.76	3.44	-0.54
135.14	675.69	684.99	3.79	-0.46
135.56	679.08	686.04	3.44	-0.54
135.61	679.46	686.16	3.79	-0.46
135.74	680.50	686.48	3.62	-0.31
135.79	680.92	686.61	2.88	-0.59
135.84	681.31	686.73	3.75	0.07
135.94	682.08	686.97	3.94	-0.48

Meters Composite Depth (mcd)	Age - ka (Channell age model)	**Age - ka (tuned to LR04)**	**δ18O (per mil)**	**δ13C (per mil)**
135.99	682.50	687.09	3.86	-0.39
136.14	683.69	687.34	3.48	-0.61
136.24	684.50	687.50	3.42	-0.53
136.29	684.92	687.59	3.48	-0.54
136.34	685.31	687.67	3.72	-0.05
136.39	685.69	687.74	3.51	-0.14
136.44	686.08	687.82	3.57	-0.02
136.49	686.50	687.91	3.62	-0.46
136.54	686.92	688.00	3.63	-0.01
136.64	687.69	688.15	3.53	0.12
136.69	688.08	688.23	3.36	-0.03
136.94	690.08	688.64	3.66	-0.18
136.99	690.50	688.73	3.62	0.33
137.49	694.46	689.85	2.83	-0.14
137.54	694.85	690.39	3.40	0.44
137.59	695.25	690.94	3.51	
137.64	695.67	691.52	3.28	0.41
137.69	696.08	692.09	3.21	0.56
137.74	696.46	692.61	3.37	0.60
137.79	696.85	693.15	3.23	0.68
137.84	697.25	693.70	3.47	0.66
137.89	697.67	694.28	2.91	0.17
137.94	698.08	694.62	2.88	-0.22
137.99	698.46	694.86	3.25	0.40
138.04	698.85	695.10	2.78	0.38
138.09	699.25	695.35	4.03	-0.58
138.14	699.67	695.61	2.86	0.41
138.19	700.08	695.96	2.75	0.51
138.29	700.85	699.22	3.03	0.14
138.34	701.25	701.09	3.48	0.61
138.39	701.67	703.06	2.96	0.80
138.44	702.08	704.92	3.17	0.29
138.49	702.46	706.44	3.23	0.30
138.54	702.85	708.00	3.69	0.45
138.59	703.25	709.58	2.79	0.32
138.64	703.67	710.72	2.83	0.93
138.69	704.08	711.69	2.96	0.74
138.84	705.25	714.24	3.13	0.55
139.04	706.85	715.34	3.83	-0.62
139.09	707.25	715.62	3.87	-0.33
139.14	707.67	715.89	3.78	-0.54
139.19	708.08	716.12	3.91	-0.62
139.24	708.46	716.34	3.90	-0.60
139.34	709.23	716.77	4.02	-0.63
139.54	710.83	717.66	3.79	-0.69
139.64	711.62	718.10	4.10	-0.68
139.66	711.73	718.17	4.08	-0.70
139.69	712.00	718.32	4.00	-0.87
139.76	712.54	718.62	3.90	-0.61
139.79	712.83	718.78	3.85	-0.69
139.84	713.23	719.00	3.99	-0.43
139.86	713.35	719.07	3.92	-0.82
139.89	713.62	719.22	3.96	-0.76
139.93	713.92	719.39	3.96	-0.98

Appendix A (continued)

Meters Composite Depth (mcd)	Age - ka (Channell age model)	**Age - ka (tuned to LR04)**	**δ18O (per mil)**	**δ13C (per mil)**
139.96	714.11	719.50	4.12	-1.18
140.03	714.64	719.79	4.03	-0.54
140.13	715.33	720.18	4.11	-0.58
140.16	715.50	720.27	4.06	-0.65
140.26	716.18	720.65	4.01	-0.86
140.28	716.36	720.75	3.93	-0.64
140.56	718.23	721.80	4.19	-0.66
141.06	721.50	723.04	4.01	-0.44
142.66	728.65	725.99	3.64	0.15
142.86	729.50	727.55	3.75	-0.40
142.96	729.93	728.34	3.83	-0.20
143.06	730.35	729.11	3.99	0.94
143.16	730.77	729.88	3.39	0.69
143.26	731.20	730.67	3.11	-0.32
143.36	731.63	731.49	2.97	-0.58
143.46	732.06	732.53	3.05	0.87
143.56	732.48	733.64	3.39	-0.30
143.76	733.38	736.04	3.79	-0.16
143.89	734.05	737.78	4.00	-0.08
143.99	734.58	739.05	3.84	-0.49
144.09	735.11	740.27	3.77	-0.37